1-1-2017

Distributed Optical Sensing in Adhesively Bonded Joints and Polymer Matrix Composite Laminates

Leeanna Meadows

Distributed optical sensing in adhesively bonded joints and polymer matrix composite laminates

By

Leeanna Meadows

A Thesis
Submitted to the Faculty of
Mississippi State University
in Partial Fulfillment of the Requirements
for the Degree of Master of Science
in Aerospace Engineering
in the Department of Aerospace Engineering

Mississippi State, Mississippi

May 2017

Distributed optical sensing in adhesively bonded joints

and polymer matrix composite laminates

By

Leeanna Meadows

Approved:

_____

Rani W. Sullivan
(Major Professor)

_____

Thomas E. Lacy
(Committee Member)

_____

Padmasiri Vipul Ranatunga
(Committee Member)

_____

J. Mark Janus
(Graduate Coordinator)

_____

Jason M. Keith
Dean
Bagley College of Engineering

Name: Leeanna Meadows

Date of Degree: May 5, 2017

Institution: Mississippi State University

Major Field: Aerospace Engineering

Major Professor: Dr. Rani Sullivan

Title of Study: Distributed optical sensing in adhesively bonded joints and polymer matrix composite laminates

Pages in Study 77

Candidate for Degree of Master of Science

As the use of polymer matrix composites for structures increases, there is a growing need for monitoring these structures. Distributed strain sensing using optical fibers shows promise for monitoring composite structures due to optical fiber's small size, light weight, and ability to obtain continuously distributed strain data. This study investigates the feasibility of using embedded optical fibers using two case studies: embedding the fibers in the adhesive layer of double lap shear composite specimens, and within composite end-notched flexure specimens to locate a growing crack front. To establish a repeatable fabrication methodology, manufacturing techniques for embedding the optical fibers were investigated. The measured strain distribution from the optical fibers compares well with data obtained from finite element analyses for both the double lap shear and end-notch flexure specimens. Additionally, the embedded optical fibers do not seem to impact the failure loads or fracture behavior of the specimens.

ACKNOWLEDGEMENTS

First, I would like to thank my advisor, Dr. Rani W. Sullivan, for all her constant guidance and support, and Dr. Vipul Ranatunga and Dr. Thomas E. Lacy for serving on my thesis committee.

This study was conducted at the Air Force Research Laboratory (AFRL) in Dayton, Ohio through the Summer Faculty Fellowship program. I am grateful for the support from both the AFRL and the University of Dayton Research Institute (UDRI). I would also like to thank Dr. Vipul Ranatangu (AFRL), Keith Vehorn (UDRI), Kevin Brown (AFRL), Dr. Steve Olson (UDRI), and Todd Bussey (AFRL) for their help during experimental testing as well as their continued guidance through regular telecom meetings.

TABLE OF CONTENTS

LIST OF TABLES

LIST OF FIGURES

CHAPTER I

INTRODUCTION

Polymer matrix composites are being used for aerospace structures more frequently due to their many attributes, such as a high strength to weight ratio, corrosion resistance, and tailorability. However, composite structures possess very complex damage mechanisms, such as a combination of matrix cracking, fiber breakage, and delaminations, which are often very difficult to detect and analyze. In many cases the damage may not be visible to the naked eye. Therefore, there is a growing need for structural health monitoring (SHM) techniques capable of detecting, locating, and analyzing the severity of different types of damage. New SHM methods could allow real-time monitoring and condition-based maintenance to replace schedule-based maintenance, creating much safer and cost efficient maintenance schedules for composite aerospace systems [1].

1.1 Fiber Optic Sensors for Structural Health Monitoring Applications

A wide variety of sensors have been implemented in SHM methods including fiber optic sensors, strain gauges, acoustic emission sensors, accelerometers, etc. Glass optical fibers have the potential to significantly reduce the complexity of strain measurement systems due to their small diameter and light weight [2]. Additionally, these fibers can be embedded directly into composite structures to obtain the actual strain distribution ([3] [4] [5] [6]). In contrast, a traditional strain gauge, surface mounted only

with heavy electrical wires, collects data only at the point of attachment. Figure 1.1 shows eight strain gauges and a single optical fiber (barely visible) that are mounted to a cantilever beam. The strain gauges and bulky wiring (red, white, and black wires) provide only eight points of measurement at a particular gauge length and spacing. In comparison, a quasi-continuous strain distribution can be obtained from the optical fiber which is equivalent to approximately 50 strain sensors.

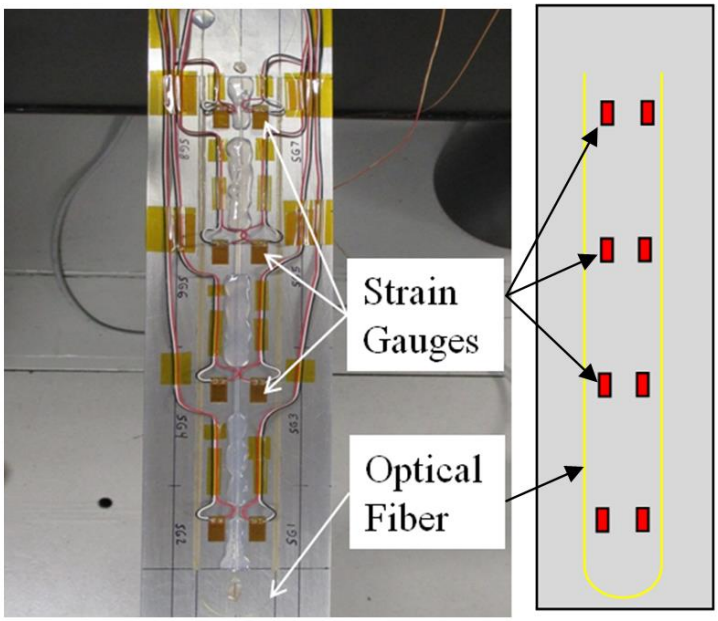

Figure 1.1 Comparison of strain gauges to a single optical fiber

Various optical fiber sensors [2] have been studied for a wide variety of SHM applications [7]. They are commonly used for monitoring physical and chemical changes in civil engineering structures [8], including bridges, buildings, pipelines, tunnels, and dams [9]. These sensors are also becoming more popular for aerospace applications. Guo et. al [2] proposes the use of fiber Bragg grating (FBG) sensors for load monitoring and

detecting damage in air platforms. Kressel et. al [10] utilized the concept of embedded FBGs to monitor the structural behavior of UAV tail booms in real time during flight. Boom overloads and local buckling were detected by tracking changes in vibration modes using the FBG data. Other large scale applications include wind turbine blade fatigue testing [11], pressure monitoring in submarine pipelines [12], and bird strike event monitoring in a composite UAV [13].

Fiber optic sensors have also been used in many small scale case studies to develop more robust SHM systems. Adhesively bonded single lap shear (SLS) specimens have been used to study the use of optical fiber sensors for monitoring adhesive layers. Canal et. al [14] embedded FBGs in composite laminates, composite/adhesive interfaces, and adhesives to monitor the strain distribution (six data points) in the bonded region of SLS specimens, and no adverse effects from the embedded fibers were observed. Capell et. al [15] used FBGs embedded two plies away from the adhesive layer to monitor disbond initiation and growth in fatigue loaded, glass fiber reinforced plastic SLS specimens through the relaxation of residual thermal strains that formed during the cure cycle. FBG sensors have also been used to monitor damage such as delamination growth in composite end-notched flexure specimens [16] [17], and fatigue crack growth in SLS specimens [18]. In this study, the feasibility of using embedded distributed optical fibers is investigated using two case studies: embedding the fibers to characterize the adhesive layer of composite double lap shear specimens [5], and within composite end-notched flexure specimens to locate and map the growing crack front due to three-point bend tests [6].

1.2 Distributed Optical Sensing

Distributed optical fiber sensors are being increasingly used for measurement of strains [19] [4] and temperatures [20]. With a single glass optical fiber, near continuous strain data can be acquired along the entire fiber length in near real time. Many fiber optic sensing applications have been developed utilizing point sensor FBGs which require etching the fiber with a grating profile to create a variation of the refractive index [2]. FBGs collect measurements only where the etching is present while distributed fiber optical sensors using optical frequency domain reflectometry (OFDR) collect measurements along the entire length of an off-the-shelf, unmodified glass optical fiber.

OFDR technology works by transmitting light into the fiber by a tunable frequency laser and measuring the back-scattered light from the natural refractive index variations along the fiber (Rayleigh scattering). With changing temperature or strain, the fiber stretches or expands causing changes in the local Rayleigh pattern. To convert these changes to local strain or temperature values, the optical fiber is divided into segments for small windows of analysis as shown in Figure 1.2a and converted to the frequency domain as illustrated in Figure 1.2b. When the segment is further away from the detector, a higher frequency of interference is observed; thus, the reflected frequency shift is proportional to the changing external conditions. The analysis window is applied to each section of the fiber by a software algorithm to obtain continuous strain or temperature measurements.

The frequency data can be post-processed with varying window sizes and locations which allow strain or temperature measurements to be obtained for any gauge length and spacing greater than or equal to 1 mm from a single data collection [19] [21].

The finest resolution (1 mm gauge length and spacing) results in a very noisy strain profile; thus, for these studies, the fiber data was post-processed with either a 3 mm gauge length and 3 mm spacing as shown in Figure. 1.3a or a 3 mm gauge length and 1 mm spacing as shown in Figure 1.3b. The 3 mm gauge length and 3 mm spacing results in a continuous strain profile with a reasonable post-processing time. The 3 mm gauge length and 1 mm spacing produces strain measurements that overlap. This creates a smoother profile with a finer resolution but requires much more processing time.

This study used the LUNA ODiSI-A [22] fiber optic sensing system. An off-the-shelf single mode 155 μm diameter optical fiber with a protective polyimide coating was used for all optical fiber test articles.

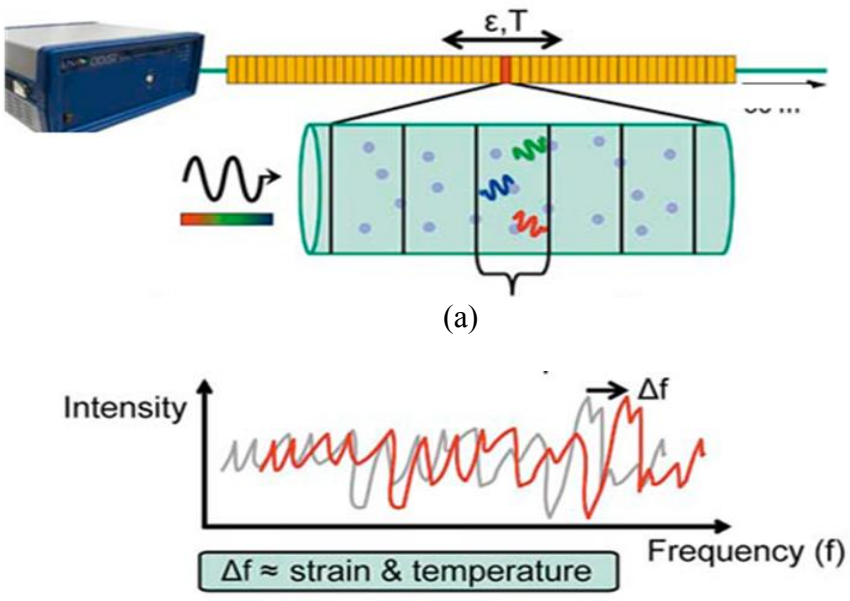

Figure 1.2 Optical frequency domain reflectometry (a) showing the signal from a small segment that is converted to (b) the frequency domain [21]

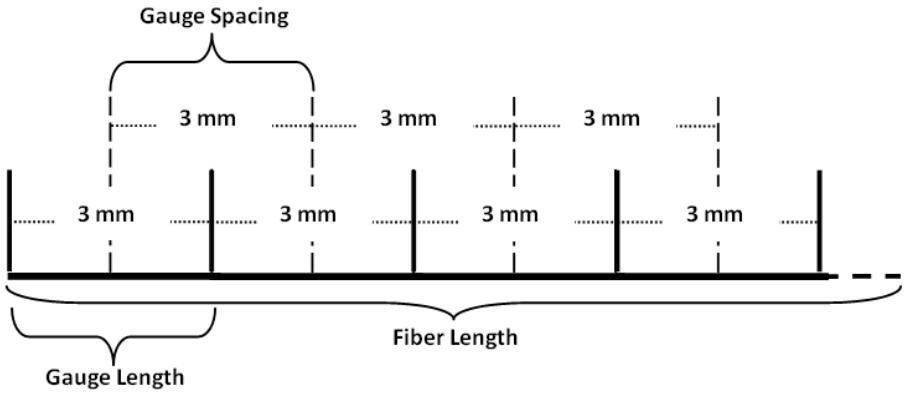

(a)

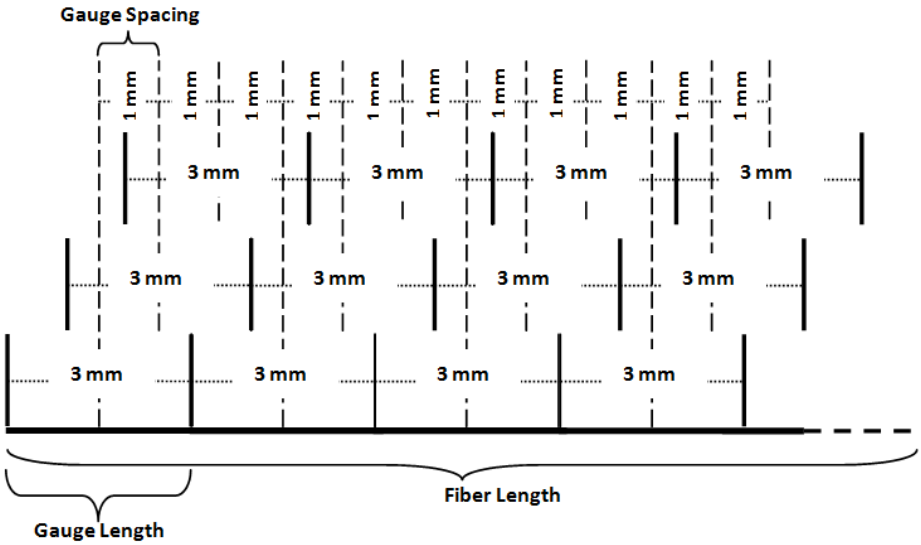

(b)

Figure 1.3 Post processing gauge length and spacing

1.3 Motivation and Objectives

The primary objective of this study was to investigate the feasibility of using embedded optical fibers for SHM applications through observing and understanding changing strain fields. Two idealized case studies were performed.

The goal of the first case study was to characterize the adhesive layer in tensile loaded composite double lap shear (DLS) specimens by embedding optical fibers directly in the adhesive layer. Adhesive bonds are often used to join composite structures; thus, obtaining an accurate monitoring system for inaccessible locations. This type of study can provide information to improve the design of composite joints and monitor the adhesive layers during service.

The second case study utilized composite end-notched flexure (ENF) test specimens with embedded optical fibers to establish a method for locating the growing crack front. This method provides a way to detect and analyze interlaminar delaminations, which are a common damage mechanism in composites.

For both case studies it was important to determine if the optical fibers affected the failure loads of the specimen. Additionally, repeatable fabrication methodologies for embedding the fragile optical fibers in test specimens were investigated

1.4 Research Scope

To meet the objectives of this study, the following tasks were completed and are further described in the indicated sections:

Bonded composite:

- Fabrication techniques for embedding optical fibers in the adhesive layer of DLS specimens were established. (Section 2.1.2)
- Failure loads for DLS specimens with embedded optical fibers were compared to those with no optical fibers to determine the effect of the optical fibers on the bond strength. (Section 2.2.1)

- The optical fiber data was post-processed to obtain the strain distribution in the adhesive layer for various tensile loads (Section 2.2.2)
- A finite element model was developed to verify the measured strain distribution obtained from the optical fiber embedded in the adhesive layer. (Section 2.2.3)

ENF composite:

- Fabrication techniques for embedding optical fibers in the composite laminates during the layup process of ENF specimens were established. (Section 3.1.2)
- The mode II fracture toughness values for composite ENF specimens with and without fibers were compared to determine if the fibers affected the composite laminate strength. (Sections 3.1.3 and 3.2.2)
- The optical fiber data was post-processed to obtain the strain distribution in composite ENF specimens. (Section 3.2.3)
- A finite element model was developed to verify the measured strain distribution obtained from the optical fiber embedded in the laminate. (Section 3.2.4)
- The crack front was located for each ENF test by examining the changing strain field and was compared to the true crack front location. (Section 3.2.6)

CHAPTER II

DISTRIBUTED OPTICAL SENSING IN COMPOSITE LAMINATE ADHESIVE BONDS

The feasibility of using embedded optical fibers to characterize the axial strain in the adhesive layer of composite joint specimens was investigated. Double lap shear (DLS) specimens with embedded optical fibers were tensile tested to obtain the axial strain of the adhesive layer and to determine the impact of the optical fibers on the bond strength [5]. The manufacturing techniques for embedding the fibers are also presented.

2.1 Double Lap Shear Specimen Fabrication and Testing

2.1.1 Description of Test Articles

DLS specimens were fabricated following ASTM D 3528-96 type B specimen [23]. Two adherends are joined by two straps each attached with a layer of paste adhesive to form the DLS joint, as shown in Figure 2.1a. An optical fiber was embedded in each of the adhesive layers such that the fiber made three passes (Pass 1, Pass 2, and Pass 3) through the adhesive as shown in the top-down view in Figure 2.1b.

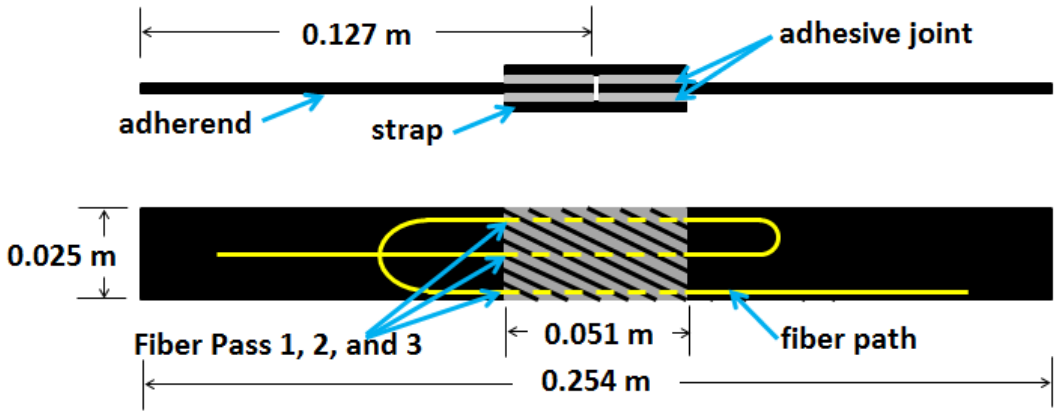

Figure 2.1 Schematic of DLS type B specimen with embedded optical fibers (a) side view and (b) top-down view

Unidirectional ($[0]_{11}$) composite adherends and straps were fabricated and cured from carbon-fiber/epoxy prepreg from Hexcel Corporation IM7 fibers and Cytec Industries, Inc. 977-3 epoxy resin [24]. Hysol® EA 9394 [25] paste adhesive was used to bond the composite components. The average post-cure adhesive layer thickness was measured to be 0.66 mm. The material properties of the specimen components are given in Table 2.1

Table 2.1 Engineering properties of DLS materials

Material Properties	**Composite Prepreg IM7/977-3** [24]	**Adhesive EA 9394** [25]
E_{11}	158 GPa	4.21 GPa
$E_{22} = E_{33}$	8.644 GPa	4.21 GPa
$G_{12} = G_{13}$	4.66 GPa	1.53 GPa
G_{23}	4.95 GPa	1.53 GPa
$\nu_{12} = \nu_{13}$	0.33	0.37
ν_{23}	0.25	0.37

2.1.2 Fabrication Procedure

Six DLS specimens (three with embedded optical fibers and three without) were fabricated and machined from a panel. Fabrication of the DLS panel involved a two-step process, with adhesive applied to each side of the panel and cured separately. To construct the DLS panel, a square unidirectional cured composite laminate ($[0]_{11}$) was cut into two 0.127 m X 0.305 m adherend sections and two 0.051 m X 0.305 m straps as shown in Figure 2.2. Prior to panel assembly, the peel plies were removed from the laminates to provide an acceptable surface for bonding. A template showing the specimen dimension, overlap region, and fiber layout was used for marking the correct placement of the optical fiber on the composite panel. A thin layer of adhesive was manually applied to one side of the adherend bond area and the panel was placed in a fixture to maintain alignment of the adherends and correct dimensions.

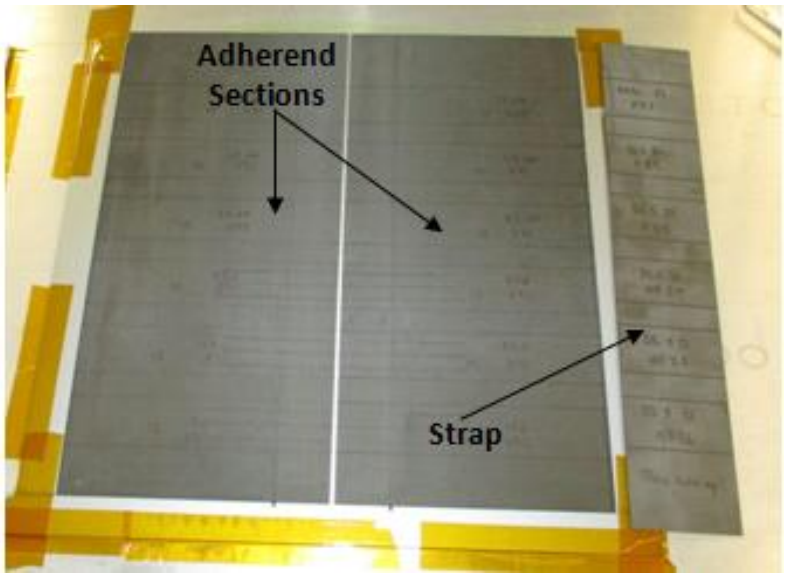

Figure 2.2 DLS specimen panel components

Optical fibers are very fragile in nature, so special care must be taken to insure the fibers survive the specimen fabrication process. An optical fiber was carefully placed on the marked fiber path, held in slight tension, and taped in place as shown in Figure 2.3. This is important since the fibers measure strain only in the axial direction. An additional thin layer of adhesive was placed on the laminate strap which was then placed on the marked overlap area and secured with tape. This insured the fiber was completely embedded in the adhesive layer. The remaining length of fiber was secured with tape on the flat laminate to avoid optical fiber breakage during the adhesive curing process.

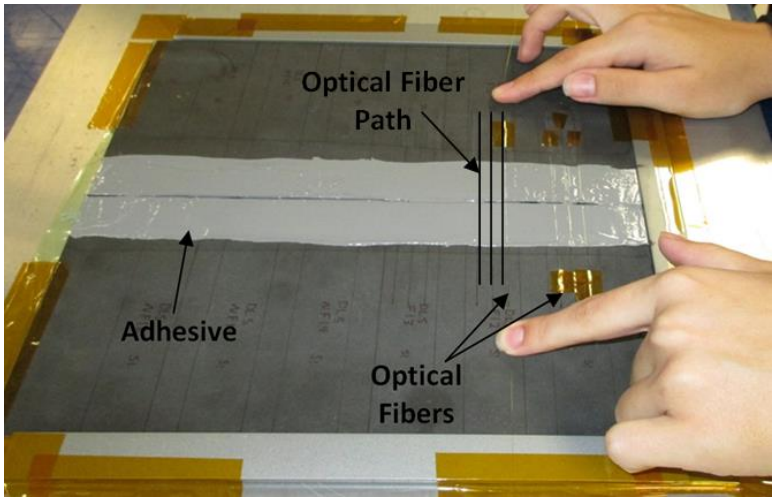

Figure 2.3 DLS specimen panel assembly

The panel was vacuum bagged with a pressure of about 10.18 in Hg (5 psi) to help maintain a constant bond line thickness and oven cured at 51.7 °C (125 °F) for 2 hours. Since optical fibers were embedded in both adhesive layers to keep each adhesive layer the same, each side of the panel was completed and cured separately. This process was repeated for the other side to complete the panel fabrication. A total of six

specimens, three with optical fibers and three with no fibers, were cut from the single panel. The six DLS specimens were carefully machined from the panel with the fibers secured onto the panel using tape.

2.1.3 Instrumentation and Testing

Prior to testing, LUNA connectors were spliced to the ends of one adhesive layer's optical fiber for each DLS specimen in preparation for connection to the LUNA system. This step was performed last to prevent damage to the connectors during the manufacturing and curing processes. The fiber was keyed to establish the length of the fiber that the LUNA system scans for measurement. Baseline fiber strain data was collected prior to each specimen test to zero the strains before loading. All tests were conducted at room temperature.

The specimens were tested in tension using an Instron Model [26] test frame with a 48.9 kN capacity. Each specimen was secured in the test frame as shown in Figure 2.4, and the fiber was connected to the LUNA system. All tests were conducted under displacement control of 0.011 mm/s. Strain data from the one adhesive layer's entire length of the fiber was acquired every 1.25 seconds until specimen failure.

During tensile testing, the LUNA system processed the data to 10 mm gauge length and spacing to obtain a near real-time view of the axial strain distribution in the optical fiber throughout the test. During post-processing, any gauge length and spacing along the fiber can be specified.

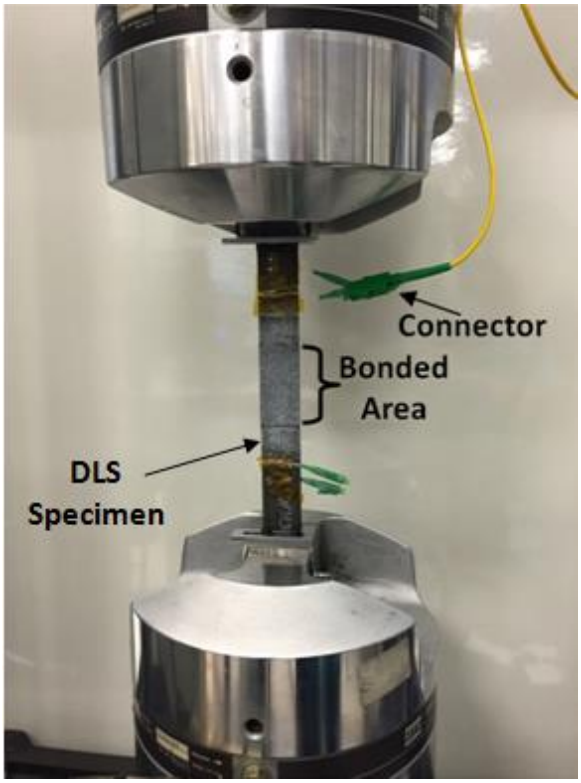

Figure 2.4 DLS experimental setup

2.2 Double Lap Shear Specimen Results and Discussion

2.2.1 Impact of Fibers on Adhesive Strength

The tensile failure loads for the six DLS specimens were recorded to determine the effect of the embedded optical fiber on the adhesive bond strength. These failure loads are reported in Table 2.2 and plotted in Figure 2.5, with Fiber1, Fiber2, Fiber3 being the specimens with the embedded optical fibers and NoFiber4, NoFiber5, and NoFiber6 being specimens without optical fibers. The average failure load of the specimens with embedded optical fiber was 4% higher than those without embedded optical fiber. However, a specimen with no embedded optical fiber failed at the lowest load. Thus, from the tests performed, the fibers did not seem to impact the strength of the

bond. The difference in the average values is most likely due to experimental variation; however, more test specimens are needed to verify this conclusion.

Table 2.2 DLS specimen tensile failure loads

Specimen	Failure Load (N)
Fiber1	15289
Fiber2	16014
Fiber3	14808
NoFiber4	14701
NoFiber5	16948
NoFiber6	16378
Average with fiber	15370
Average with no fiber	16009
Standard Deviation	903

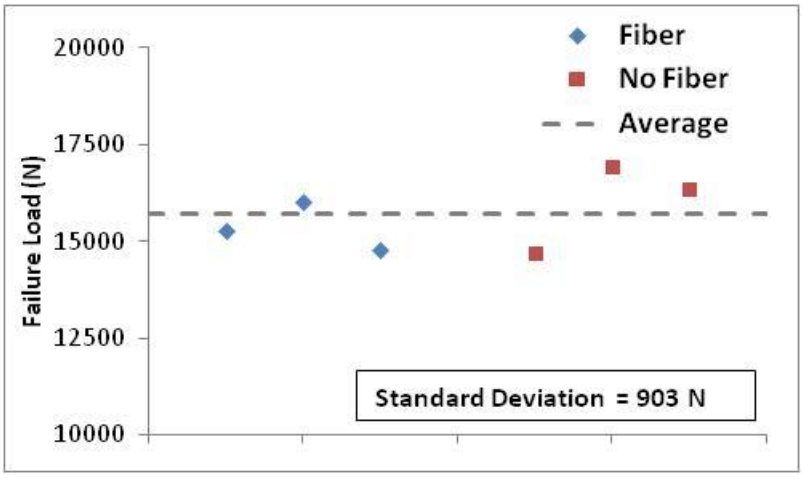

Figure 2.5 DLS specimen tensile failure loads for specimens with and without embedded optical fibers

2.2.2 Strain Measurements in Adhesive Layer

For this study, a 3 mm gauge length and spacing was chosen for post processing of the optical fiber strain data, resulting in a reasonable processing time and a resolution that provided approximately 16 strain data points for each optical fiber pass through the adhesive layer of each specimen resulting in a total of 50 strain points over the two inch bonded area.

Figure 2.6 shows three sample strain distributions at three different loads (2000 N, 4000 N, 6000 N) from three fiber passes through one of the adhesive layers of a DLS specimen. Sharp spikes appear at the ingress/egress points where the fiber enters and exits the bond line. The distance between the ingress and egress points is 0.051 m which corresponds to the joint length of the specimen (Figure 2.1). A center spike is also seen between the ingress/egress points which corresponds to the butt joint in the double lap shear specimen. In between the fiber passes is the region where the optical fiber loops outside of the adhesive layer where the strain is approximately zero. The corresponding loads are approximate values obtained by correlating the load displacement data from the test frame to the fiber data time stamp.

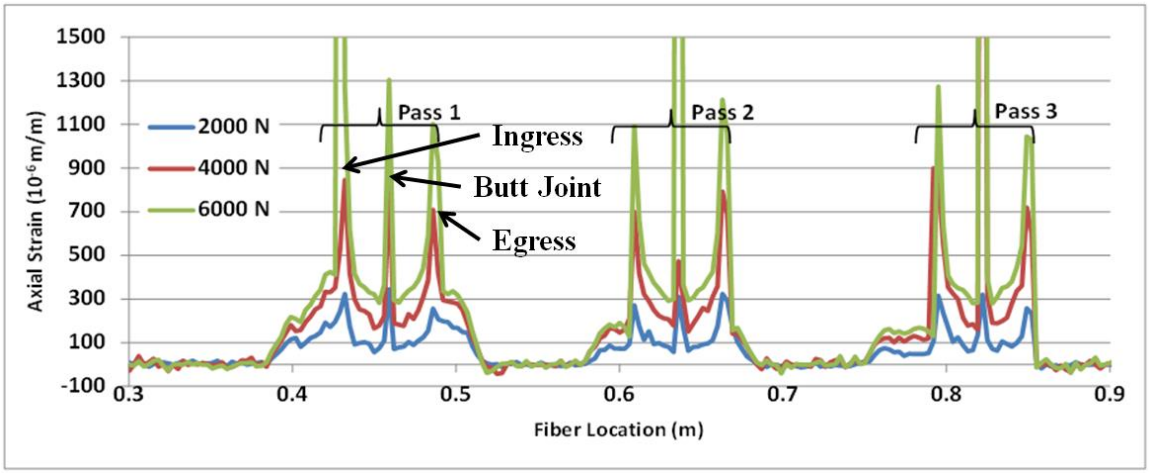

Figure 2.6 DLS-Fiber3 sample strain data from embedded optical fibers

To observe the strain distribution across the width of a joint, the strain data for each pass from 9 mm inside the adhesive layer was plotted as shown if Figure 2.7. The strain is fairly uniformly distributed and shows a linear relationship with the increasing load. Some deviation between the fiber passes is seen at the high loads. This may be indicative of slight twist prior to failure resulting in slightly higher strains on one side.

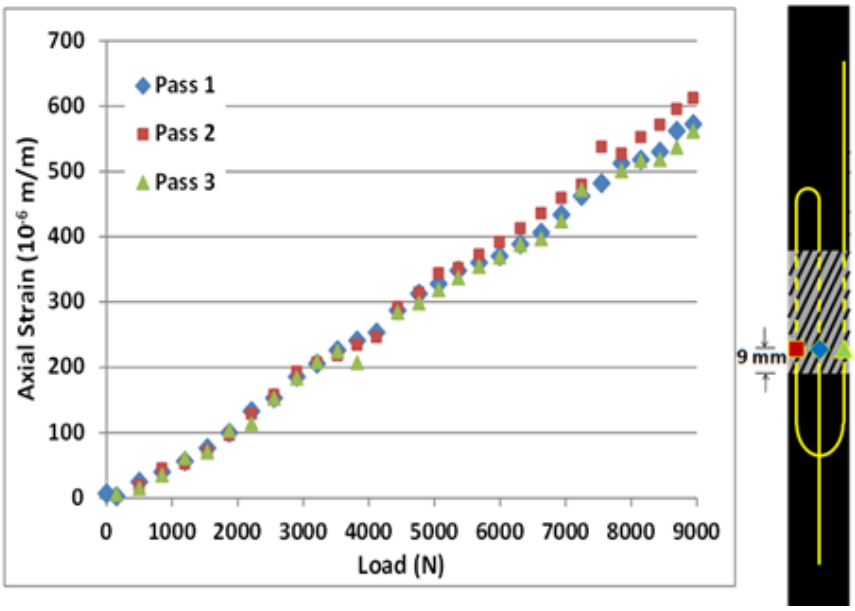

Figure 2.7 DLS-Fiber3 strain versus. load for each fiber pass 0.009 m inside bond line

In Figure 2.8, the strain data from the three fiber passes are superimposed to demonstrate the strain distribution in the adhesive layer as the load increases. At the loads of 1200 N (Figure 2.8a) and 3500 N (Figure 2.8b), and 6300 N (Figure 2.8c), comparing the strain from pass 1, 2, and 3 shows the strain is fairly uniform across the width of the specimen and has the bowl shaped distribution expected in the adhesive layer [4]; the ingress and egress points are clearly shown by the high strains at -0.027 and 0.027 m, and the butt joint at 0 m. In comparison, Figure 2.8d shows the strain in the overlap within 1.25 seconds from failure (8950 N); here the high strains at the ingress, egress, and butt joint indicate slight peeling at the adhesive interface occurring the instant before failure. Strain distributions for some additional DLS specimens are found in Appendix A.

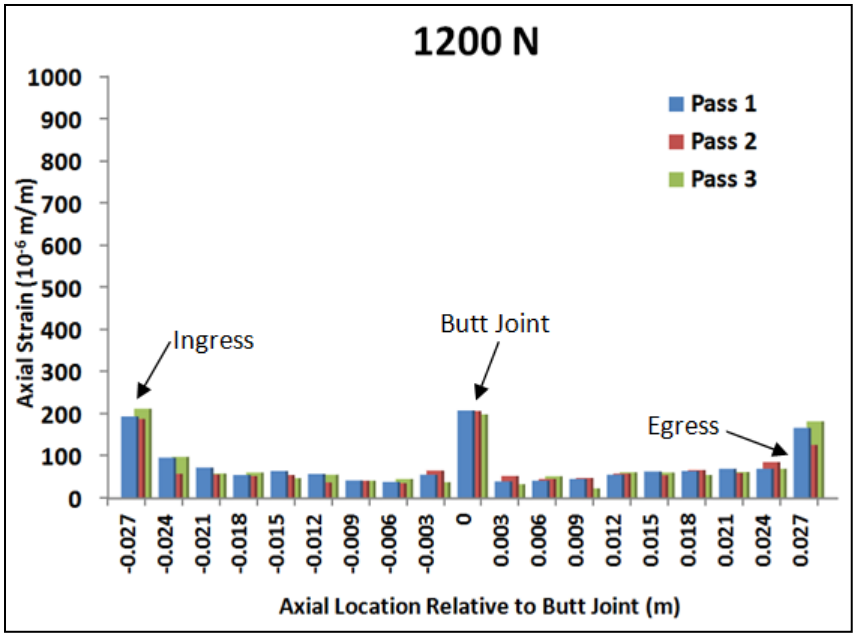

(a)

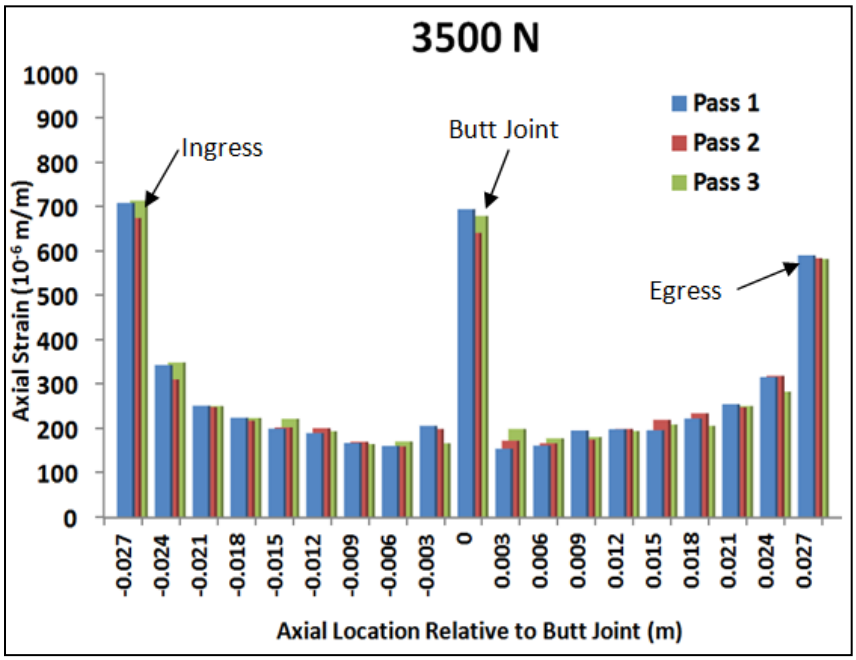

(b)

Figure 2.8 DLS-Fiber3 strain distributions at (a) 1200 N, (b) 3500 N, (c) 6300 N, and (d) 8950 N (near failure)

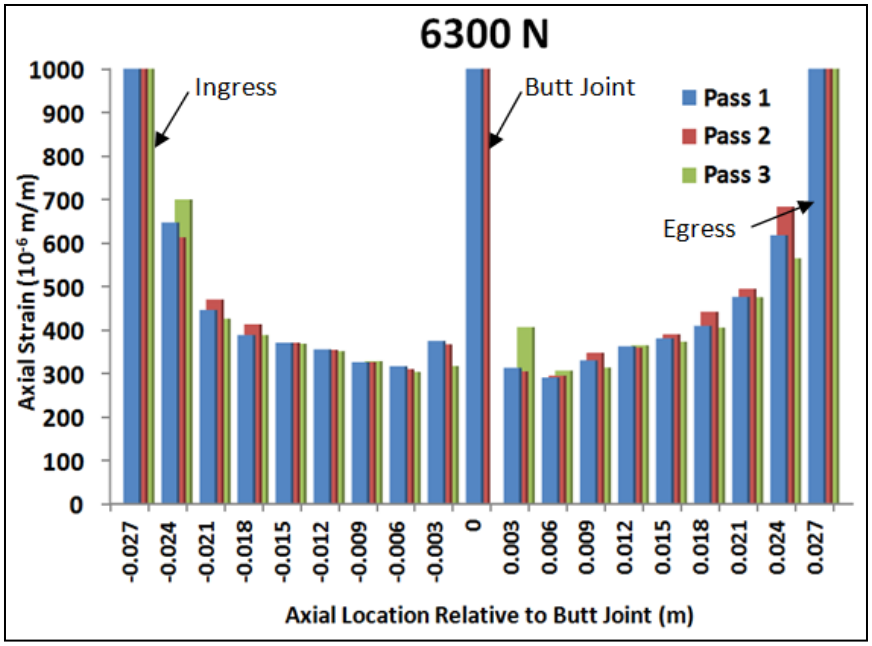

(c)

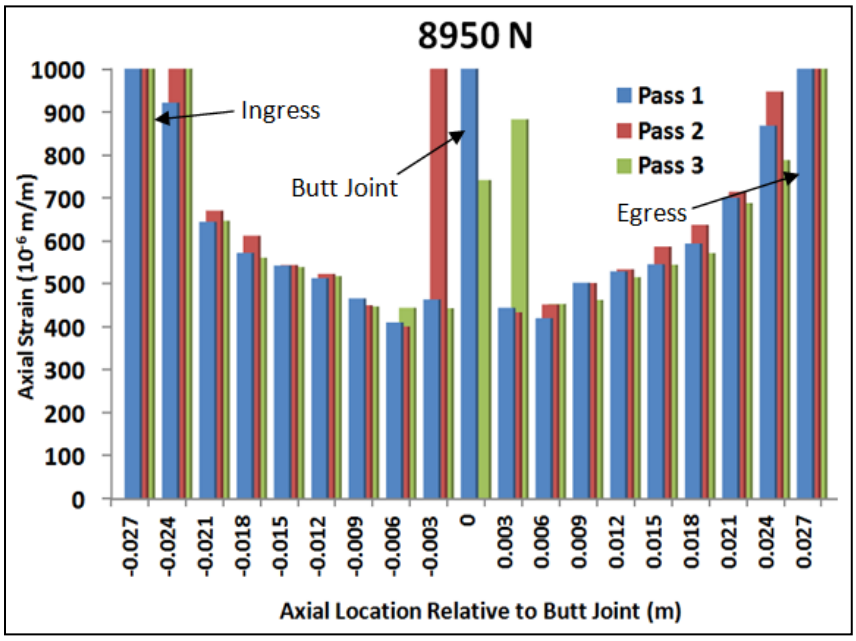

(d)

Figure 2.8 (continued)

2.2.3 Finite Element Strain Comparison to Optical Fiber Measured Strain Data

To verify that correct measurements were being obtained from the optical fibers, the strain distribution was compared to numerical results. A finite element (FE) model of a DLS specimen without embedded optical fiber was created using a linear elastic analysis in Abaqus [27] as shown in Figure 2.9. The material properties used in the model are listed in Table 2.1. A 1/8 model exploiting symmetry was created using 3.1M elements (C3D8R hexahedra), 3.4M nodes, and 10.2M degrees-of-freedom.

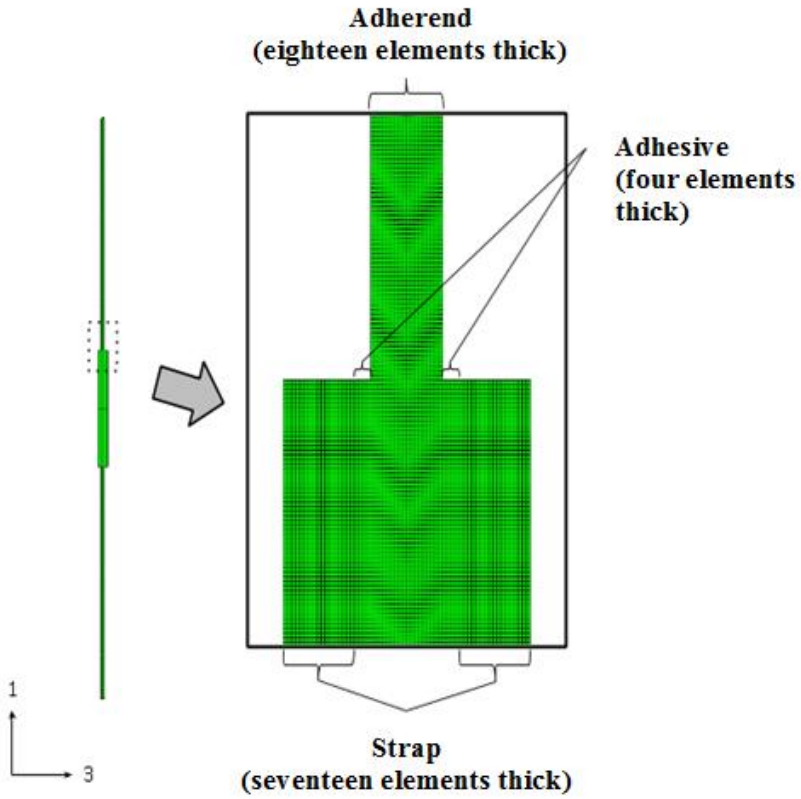

Figure 2.9 DLS FE model

Figure 2.10 shows the optical fiber measured strain data from all three fiber passes at 3500 N plotted with the strains obtained from the FE model at the center of the

adhesive layer. The measured strain distribution from the optical fibers compares well with data obtained from the FE model. Singularities appear at the ingress/egress and butt joint, and the same bowl shaped distribution appears in both the experimental and FE data. At the ingress/egress points, the singularities are negative in the FE data and positive in the fiber data which causes the mismatched data.

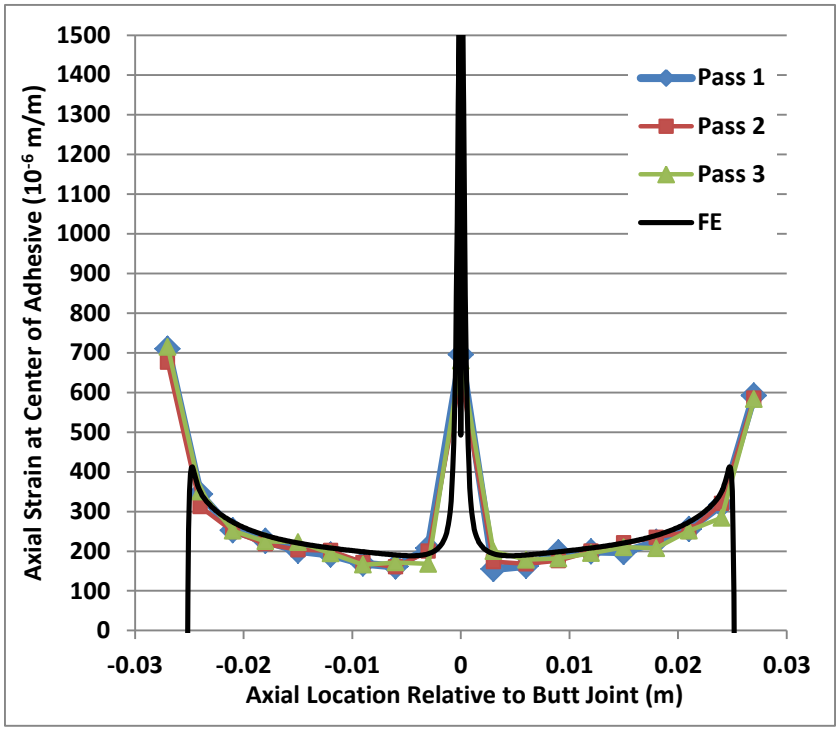

Figure 2.10 DLS FE comparison to optical fiber strain data at 3500 N

CHAPTER III

DISTRIBUTED OPTICAL SENSING IN COMPOSITE LAMINATES

Distributed optical sensing was also used to gain insight into the complex damage of composite structures. The end-notched flexure (ENF) test, as prescribed in ASTM D 7905, was used to investigate interlaminar delamination by evaluating the mode-II interlaminar fracture toughness (G_{IIc}) for unidirectional fiber-reinforced polymer matrix composite laminates [28]. In this section a method is developed for locating the growing delamination front by observing the changing strain field from embedded distributed optical fiber sensors [6].

3.1 End-Notched Flexure Specimen Fabrication and Testing

3.1.1 Description of Test Articles

Four ENF specimens with embedded optical fiber and three without fibers were fabricated following ASTM D 7905 [28]. $[0]_{26}$ laminates were fabricated from unidirectional carbon-fiber/epoxy prepreg (Hexcel Corporation IM7 fibers and Cytec Industries, Inc. 977-3 epoxy resin). The material properties are given in Table 3.1. As shown in Figure 3.1a, optical fibers were embedded during the composite layup process and were placed at one ply offset from the delamination plane to avoid fiber breakage during testing. The fiber layout includes three passes (P1, P2, P3), shown in Figure 3.1b, through the specimen, so the crack (delamination) front shape can be determined from the

fiber strain data. A Teflon film was inserted at the midplane to form an initiation site for delamination growth.

Table 3.1 ENF specimen material properties [24]

Material Properties	Composite Prepreg IM7/977-3
E_{11}	158 GPa
$E_{22}=E_{33}$	8.644 GPa
$G_{12}=G_{13}$	4.66 GPa
G_{23}	4.95 GPa
$\nu_{12}=\nu_{13}$	0.33
ν_{23}	0.25

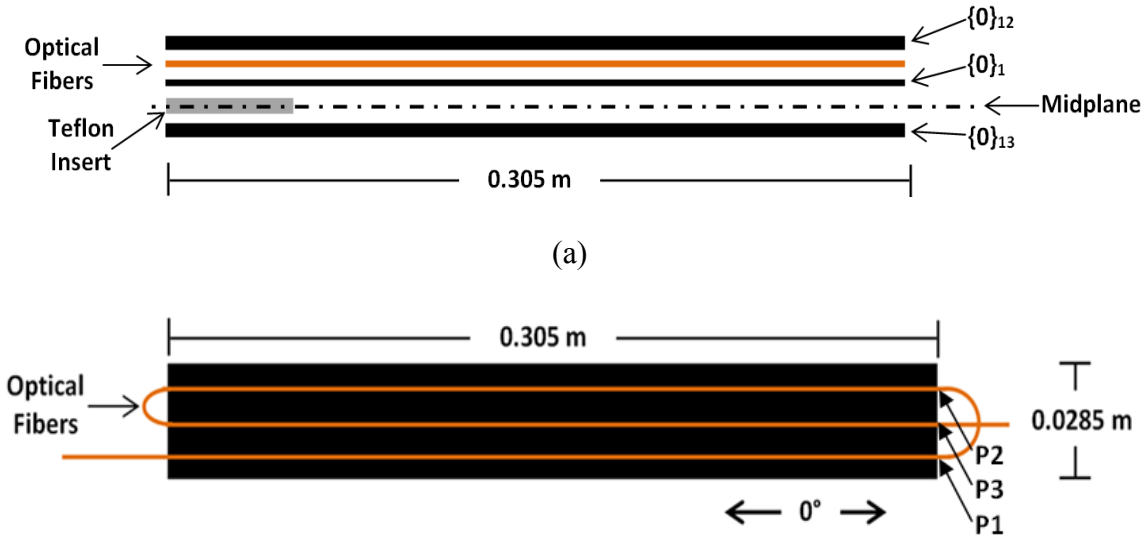

Figure 3.1 ENF specimen geometry (a) expanded side view and (b) top down view of fiber layout

3.1.2 Fabrication Procedure

Optical fibers are very fragile in nature, so special care must be taken to insure the fibers survive the ENF specimen fabrication process. The following steps outline the procedure and concerns for fabricating ENF specimens with embedded optical fibers:

1. Two pre-preg laminates each of $[0]_{12}$ configuration were laid-up.
2. The fibers were heat tacked in place on the twelve ply laminate with a heated iron tip (Figure 3.2) following the layout shown in Figure 3.1. Heat tacking ensures the fibers will remain straight and equally spaced during the layup process. A template with marked specimen and fiber locations was used (Figure 3.2) to guide the fiber placement and track the specimen locations. Since the fiber connectors may be damaged during the autoclave cure cycle (350ºF, 100 psi), an additional length of optical fiber outside the laminate was included for adding the connectors prior to testing.
3. A single pre-preg ply ([0]) was placed over the tacked optical fibers.
4. Silicon sheets (Figure 3.3) of half the laminate thickness and the specimen width were placed at the edge of the laminate underneath the fibers to keep the fibers from bending and breaking under the autoclave pressure during curing.
5. A Teflon film (Figure 3.4) was placed at the midplane to initiate delamination growth.
6. The remaining 13 pre-preg plies ($[0]_{13}$) were added to complete the layup.
7. A protective film was placed over the fibers to prevent bonding of the fibers to the peel ply and breather materials.

8. The layup was bagged and cured according to the manufacturer's specifications (350ºF, 100 psi).
9. Following the cure cycle, the bagging material was carefully removed to avoid breaking the fibers. The cured test panel is shown in Figure 3.5.
10. The final specimens (four with optical fibers and three without fibers) were carefully machined (Figure 3.6) from the panel using the template as a guide. During the placement of fibers, a 25 mm machining space was included between each specimen. This helped ensure that the fibers were not cut during machining.
11. To complete specimen fabrication, a thin layer of white paint was applied to the sides of the specimen to assist in visually locating the crack tip during testing.

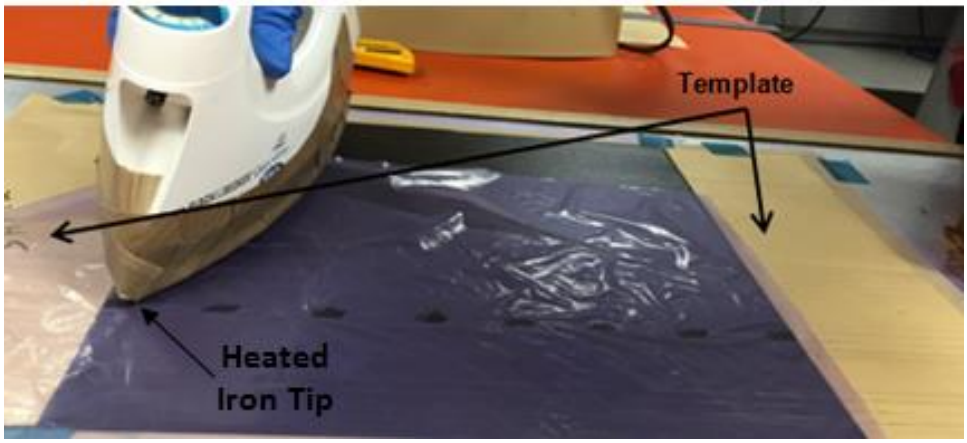

Figure 3.2 ENF specimen fabrication: heat tacking fibers using a template

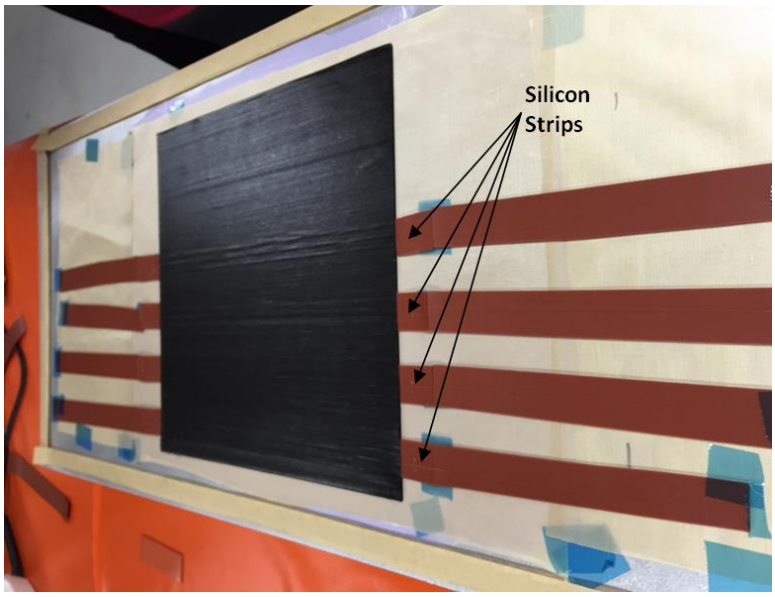

Figure 3.3 ENF specimen fabrication: silicon dams placed under optical fibers

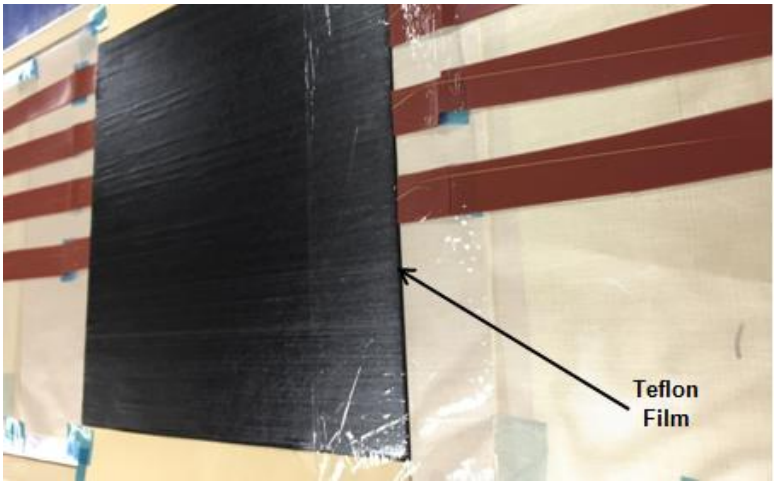

Figure 3.4 ENF specimen fabrication: Teflon film placed

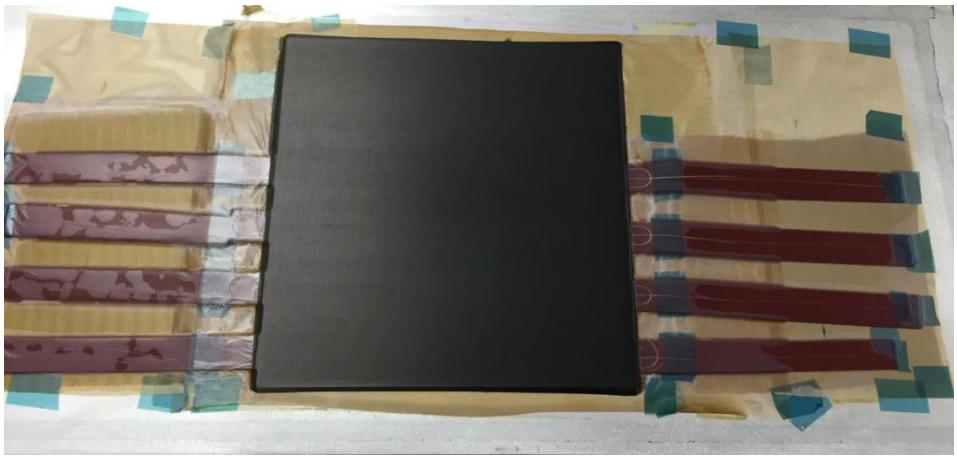

Figure 3.5 ENF specimen fabrication: cured panel

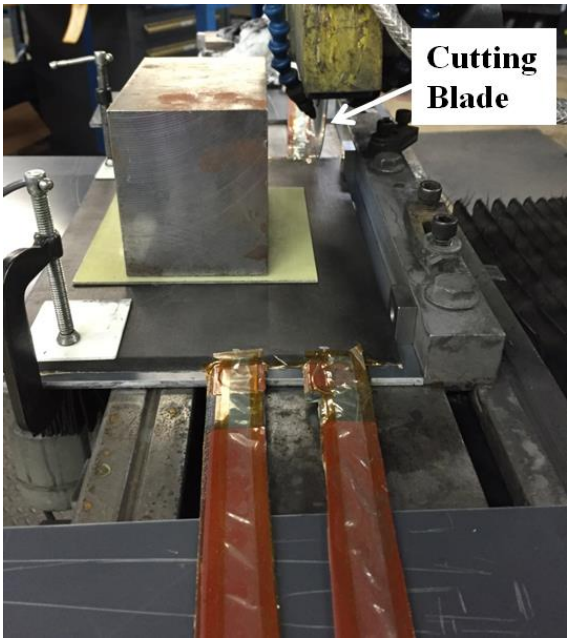

Figure 3.6 ENF specimen fabrication: specimens machined from cured panel

3.1.3 Instrumentation and Testing

Connectors were spliced to the ends of the optical fibers of each ENF specimen in preparation for connection to the LUNA system. This step was done last to avoid the connectors being damaged during the manufacturing and curing processes. Each fiber is keyed to establish the length of fiber the LUNA system scans for measurement. Baseline fiber strain data was collected prior to each specimen test to zero the strains before loading. All tests were conducted at room temperature.

The ENF tests were conducted following ASTM D 7905 [28] using the three-point bend test configuration shown in Figure 3.7 where a_0 is the initial distance from the left roller to the crack tip. For unidirectional fiber-reinforced polymer matrix composites, the standard [28] requires a three-point compliance calibration (CC) method and linear elastic fracture mechanics to calculate the G_{IIc} values [29]. Using a 100 kN Instru-Met Electro-Mechanical [30] load frame, the load was applied to the middle roller under displacement control with a loading rate of 0.5 mm/min. The experimental setup is shown in Figure 3.8.

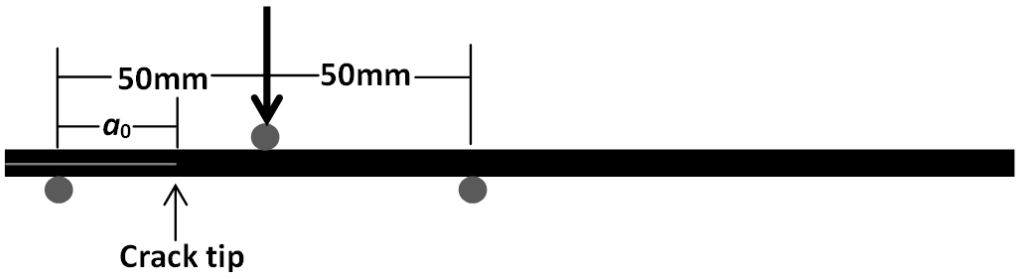

Figure 3.7 ENF test configuration

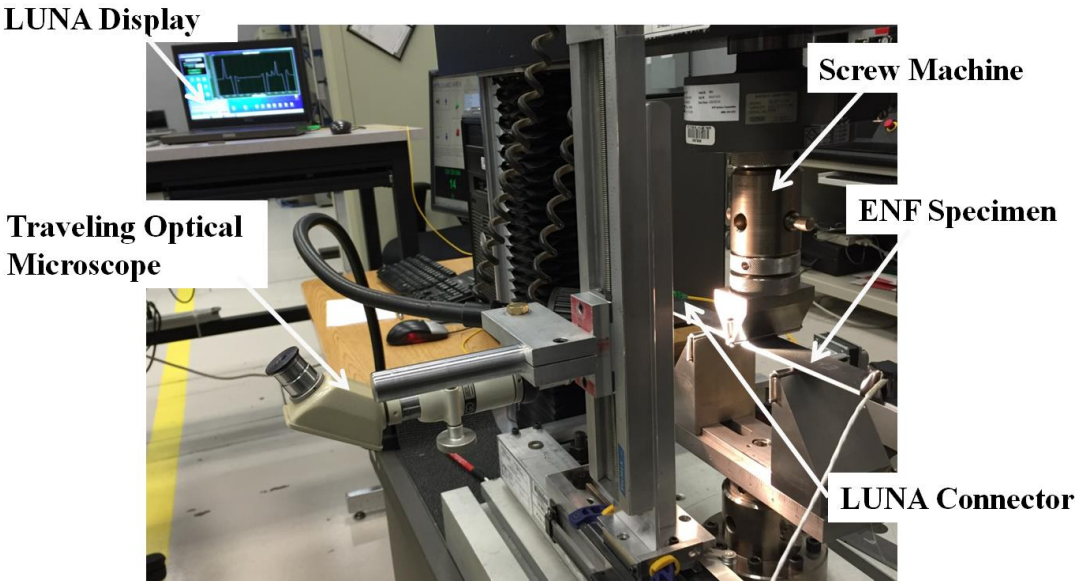

Figure 3.8 ENF experimental setup

Compliance calibration was performed for each test prior to each crack propagation by adjusting a_0 to 20 mm and 40 mm and loading the specimen to 50% of the expected critical force for the particular crack length. The CC tests for a_0 = 20 mm and 40 mm do not result in crack propagation. For crack propagation, a_0 was set to 30 mm and the load was applied until delamination growth occurred. Each new crack tip location was visually located using a traveling optical microscope and marked on the side of the specimen. Strain data was collected from the embedded optical fibers during loading and unloading for the a_0 = 30 mm case. For each initial crack length, the CC coefficients were determined by finding the slope of the linear portion of the crosshead displacement versus load curves using least squares linear regression. This is shown for a single test in Figure 3.9. The CC coefficients for this test are reported in Table 3.2. These coefficients were then plotted (Figure 3.10) to obtain the compliance, which can be expressed as

$$C = A + m{a_0}^3 \tag{3.1}$$

where A is intercept of the CC coefficient vs. crack length cubed plot, m is the slope of this curve, and a_0 is the initial crack length.

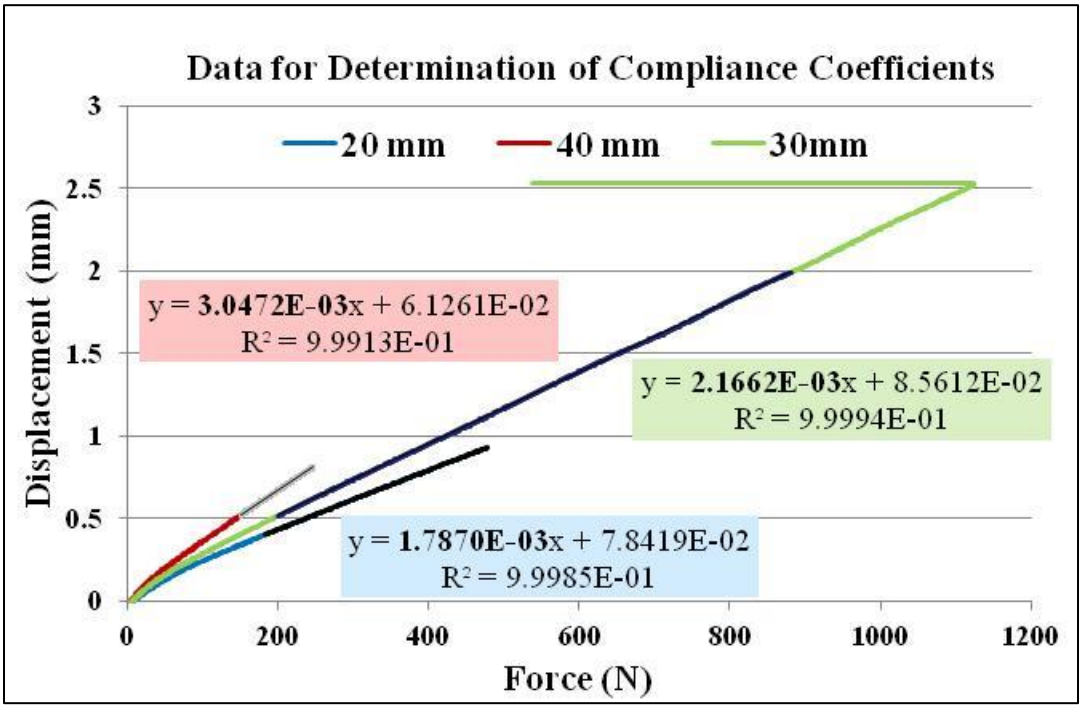

Figure 3.9 Displacement versus load data used to determine compliance coefficients for a_0 = 20 mm, 30 mm, and 40 mm

Table 3.2 Compliance calibration coefficients from sample data

a (mm)	a_0^3 (mm^3)	C
20	8000	1.79E-03
30	27000	2.17E-03
40	64000	3.05E-03

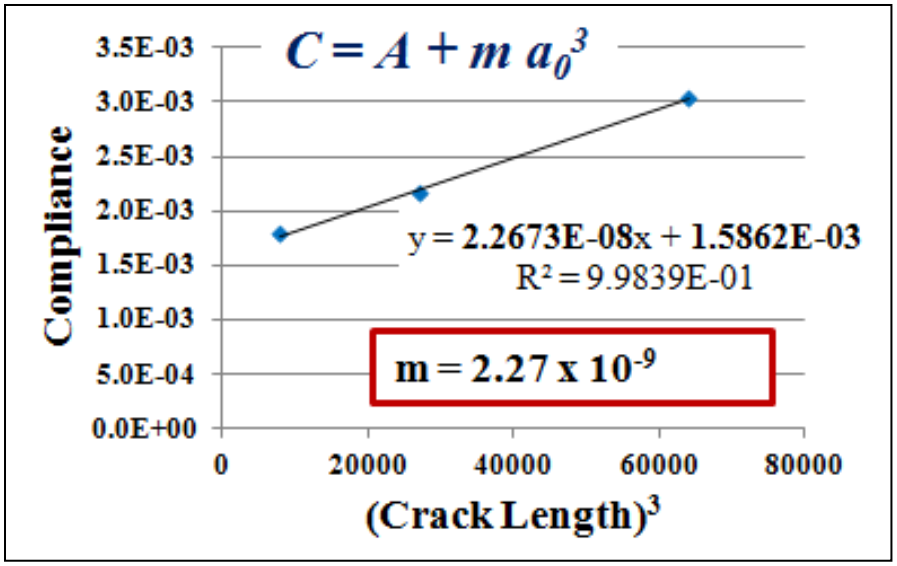

Figure 3.10 Compliance versus crack length cubed

To determine G_{IIc}, we begin from the strain energy release rate from linear elastic fracture mechanics given by

$$G = \frac{P^2}{2}\frac{dC}{da} \tag{3.2}$$

where P is the load applied in the three-point bend loading, a is the crack length, and C is the compliance from Equation 3.1. From Equations 3.1 and 3.2 and the ENF specimen geometry, G_{IIc} can be determined using

$$G_{II_c} = \frac{3mP_{max}^2 a_0^2}{2B} \tag{3.3}$$

where m is the slope in Equation 3.1, P_{max} is the peak load where crack propagation occurs, a_0 is the initial crack length (30 mm), and B is the specimen width [31].

The ENF test was repeated for each new crack tip location to obtain multiple strain data sets per specimen. Two conditions exist for each specimen: non-precracked

(NPC) and pre-cracked (PC). NPC occurs when the delamination grows from the blunt edge of the Teflon insert. Therefore, one NPC G_{IIc} value is obtained from each specimen and is higher than the PC G_{IIc} values due to greater energy required to imitate crack . PC conditions are created from the sharp crack tip after the first crack growth. Multiple PC G_{IIc} values can be obtained for each ENF specimen depending on the length of the specimen [28] [31].

3.2 ENF Specimen Results and Discussion

3.2.1 ENF Test Matrix

A total of 67 ENF tests (40 with optical fibers and 27 with no optical fibers) were performed. Table 3.3 shows the test matrix and the average pre-crack (PC) peak load for each specimen.

Table 3.3 ENF test matrix

Specimen	Optical Fiber (Y/N)	# NPC Tests	# PC Tests	Average PC Peak Load (N)	Standard Deviation (N)
ENF-101	Y	1	9	796	28
ENF-102	Y	1	9	807	11
ENF-103	Y	1	9	792	20
ENF-104	Y	1	9	661	15
ENF-NF1	N	1	8	832	34
ENF-NF2	N	1	9	798	21
ENF-NF3	N	1	7	786	30

3.2.2 Impact of Fibers on Mode II Fracture Toughness

Previous studies have shown that embedded fiber optic sensors can affect fracture behavior under certain configurations and loading conditions and reduce the strength of

the specimens [32]. To determine the impact of the embedded optical fibers on the fracture behavior, the NPC and PC G_{IIc} values for specimens with and without optical fibers were calculated as described in section 3.1.3. The resulting values for four specimens with optical fibers and three without fibers are plotted in Figure 3.11. Each specimen provides a single NPC G_{IIc} value and nine PC G_{IIc} values. The average G_{IIc} values for NPC are 1.257 kJ/m^2 with embedded fiber 1.254 kJ/m^2 without, and the average values for PC are 0.561 kJ/m^2 with embedded fiber and 0.553 kJ/m^2. Therefore, it was concluded that only experimental variation was observed and the embedded fibers do not affect the mode-II fracture toughness when the fibers are embedded parallel to the composite reinforcing fiber.

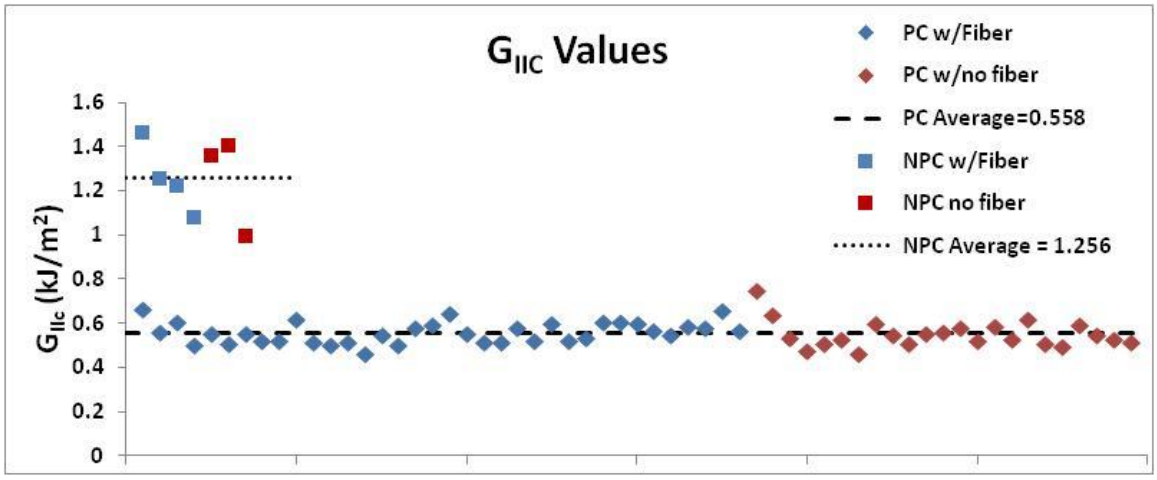

Figure 3.11 NPC and PC G_{IIc} values for ENF specimens with and without embedded optical fibers

3.2.3 Strain Measurements in ENF Specimens

Figure 3.12 shows the typical strain distribution from the embedded optical fiber before (blue line) and after (red line) the crack growth in specimen ENF-101. The green diamonds indicate where the optical fiber enters and exits the ENF specimen. The three passes through the specimen are labeled P1, P2, and P3 and are shown in the schematic in Figure 3.1. Similar distributions are seen for all three passes with the data from P2 reversed since the fiber path is in the opposite direction. Figure 3.13 shows the strain data from the first fiber. Following the before crack growth (blue) line in Figure 3.13, point A is the location of the left roller where the strain is zero. A region of high negative strain appears where the crack is present between points A and B. At point B, the strain is zero again at the initial crack tip location which was set to 30 mm from the left roller before crack growth. The strain then increases to its maximum where the load is applied by the middle roller at point C and decreases back to zero by point D at the right roller. After crack growth occurs, the crack tip location is at point E as observed from the optical microscope. For this case, the crack has grown past the middle roller (point C) which is common for the NPC condition. The difference between points B and E indicates the crack growth that occurred along the optical fiber. Thus, the crack growth length can be extracted from the optical fiber strain data. Similar strain profiles were seen from all tests and this data can be found in Appendix B.

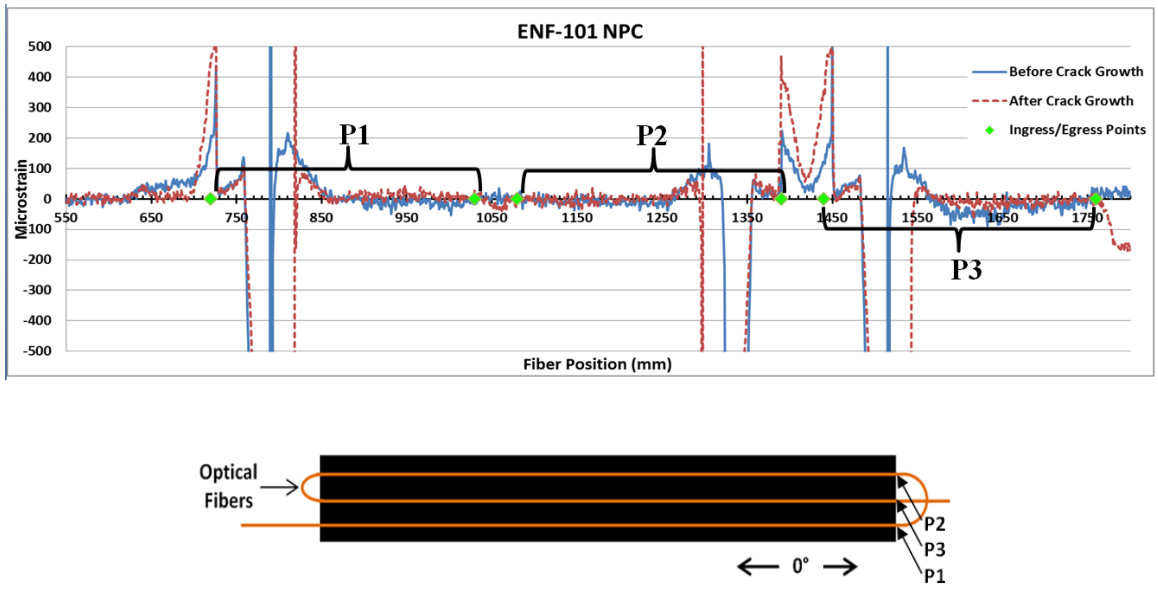

Figure 3.12 ENF-101 NPC strain data before and after crack growth

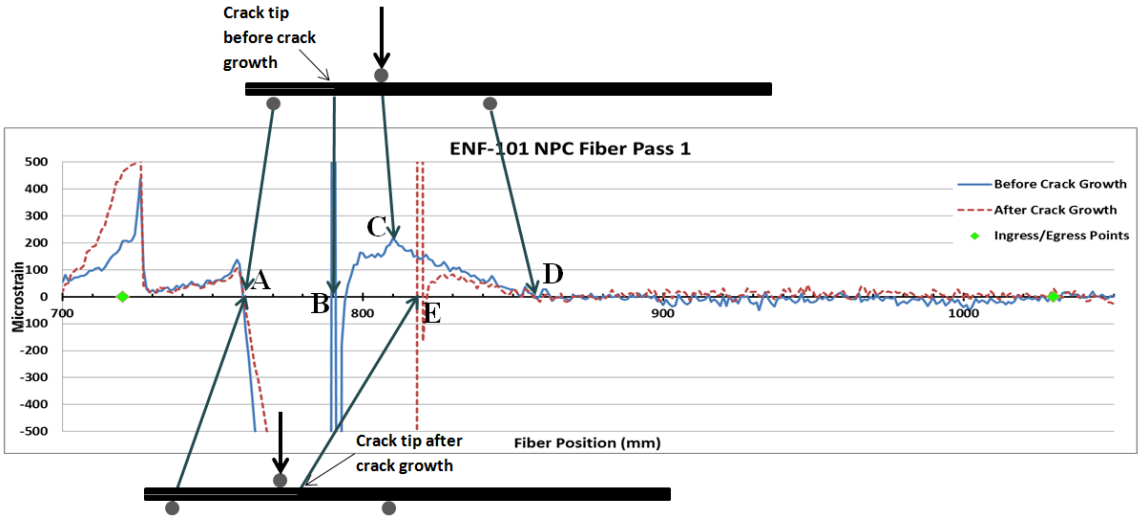

Figure 3.13 ENF-101 NPC strain data of a single fiber pass before and after crack growth

3.2.4 Finite Element Strain Comparison to Optical Fiber Measured Strain Data

To verify that correct strain measurements were being obtained from the, the strain distribution was compared to numerical results. A finite element (FE) model of an

ENF specimen without embedded optical fiber was created using a linear elastic analysis in Abaqus [27]. The material properties listed in Table 3.1 were used in the model. A 2D plane strain model exploiting symmetry was created using 27k elements and 29k nodes as shown in Figure 3.14. The three-point bend loading was simulated using analytical rigid rollers with contact constraints and the boundary conditions shown in Figure 3.14. The crack was modeled by inserting a 2D crack at the midplane.

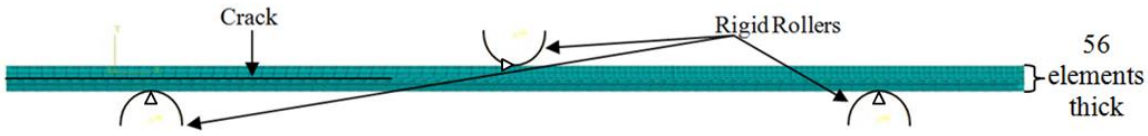

Figure 3.14 ENF finite element model

The FE strain data was reported along a line located a single ply thickness from the midplane which corresponds to the optical fiber location. Figure 3.15 shows the optical fiber strain data from ENF-101 PC1 with the results of the FE analysis. The strains are normalized by the maximum strain at the middle roller. The measured strain profile from the optical fibers compares well with the data from the FE model. The general length and shape of the crack region (location 20-55 mm) compares well with the prediction; however, there are differences that are possibly due to neglecting friction in the FE model.

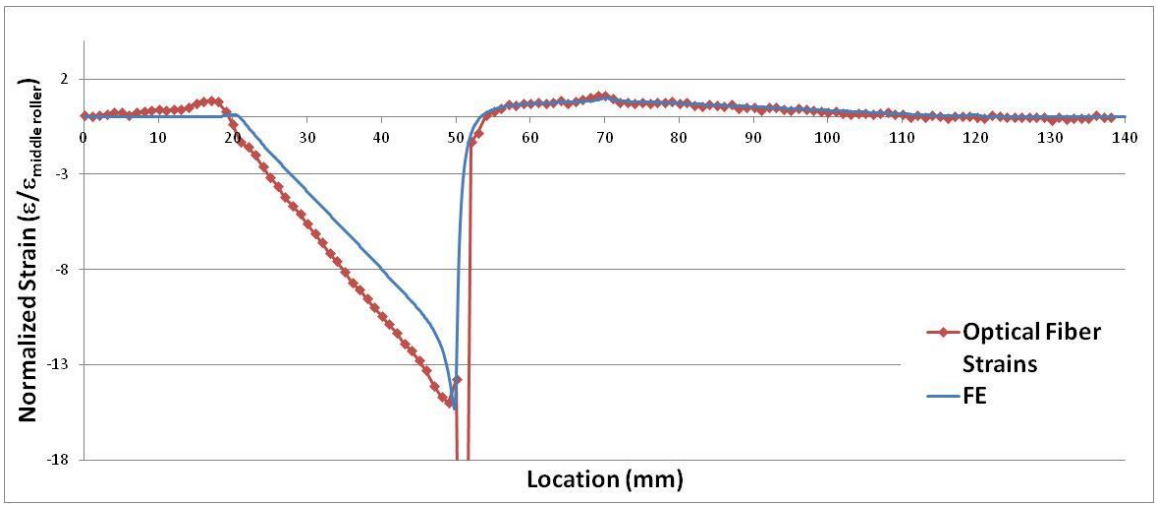

Figure 3.15 Strain from ENF finite element model compared to optical fiber strain data

3.2.5 Post-processing for Crack Growth Length

The optical fiber strain data from the LUNA was post-processed with a 3mm gauge length and 3mm spacing and a 3 mm gauge length and 1 mm spacing. The 3 mm gauge length and 3 mm spacing results in a continuous strain profile (approximately 100 strain measurements per fiber pass) with a reasonable post-processing time and a resolution that provides fairly accurate crack growth measurements; this is further discussed in the next section. The 3 mm gauge length and 1 mm spacing produces strain measurements that overlap. This creates a smoother profile (approximately 300 strain measurements per fiber pass) with a finer resolution but requires much more processing time

The fiber strain data is collected at a maximum sample rate of approximately 1 Hz during testing. This results in several strain profiles before and after crack growth, but the sample rate is not high enough to acquire the strain as the crack grows. MATLAB [33]

was used to smooth the strain data and calculate the crack growth length by finding the difference between the width of the negative strain regions before and after crack growth. Near point B in Figure 3.13, large fluctuations occur in the optical fiber measurements due to the high strain at the crack tip. The appearance of the fluctuations does not occur in every strain data collection, but occurs randomly at points of high strain which results in false values for the negative strain regions used for calculating the crack growth. Thus, the calculated crack growth values are averaged from multiple strain profiles after crack growth occurs.

3.2.6 Crack Front Mapping

To validate the calculated crack growth values, true crack growth values were compared to the optical fiber data. The true crack growth measurements were obtained by splitting open the ENF specimens after testing to view the faint lines left from the crack front progressions. Using a caliper, the true crack growth was measured to the nearest 1 mm. The following tables compare the true crack growth to the crack growth obtained from the fiber data for a single ENF specimen. Table 3.4 shows results for the 3 mm gauge length and spacing, and Table 3.5 lists the data for the 3 mm gauge length and 1 mm spacing.

Table 3.4 ENF-101 optical fiber measured crack growth (mm) for 3 mm gauge length and 3 mm spacing compared to true (caliper measured) crack growth measurements (mm)

	Pass 1		Pass 2		Pass 3 (middle)	
	true	**fiber**	**true**	**fiber**	**true**	**fiber**
NPC	28	30	27	29	27	29
PC1	15	13	16	14	16	13
PC2	14	16	15	17	15	15
PC3	17	17	17	18	18	19
PC4	14	14	14	14	14	15
PC5	16	12	16	13	16	13
PC6	13	13	14	13	14	14
PC7	14	12	15	14	15	15
PC8	14	16	14	15	14	15
PC9	14	14	14	16	14	16
				Average Difference		**1.4**
				Standard Deviation		**1.1**

Table 3.5 ENF-101 fiber measured crack growth measurements (mm) for 3 mm gauge length and 1 mm spacing compared to true (caliper measured) crack growth measurements (mm)

	Pass 1		Pass 2		Pass 3 (middle)	
	true	**fiber**	**true**	**fiber**	**true**	**fiber**
NPC	28	29	27	29	27	29
PC1	15	15	16	14	16	16
PC2	14	14	15	16	15	14
PC3	17	16	17	17	18	17
PC4	14	13	14	13	14	14
PC5	16	14	16	13	16	14
PC6	13	13	14	14	14	12
PC7	14	14	15	14	15	15
PC8	14	13	14	14	14	14
PC9	14	14	14	14	14	14
				Average Difference		**0.8**
				Standard Deviation		**0.88**

The average difference and standard deviation between the true and fiber-measured crack growth were calculated for each case. The 3mm gauge length and spacing has an average difference of 1.4 mm and a standard deviation of 1.1 mm, and the 1 mm gauge length and spacing has an average difference of 0.8 mm and a standard deviation of 0.88 mm which is slightly more accurate than the larger gauge spacing. The crack growth measurements in Tables 3.4 and 3.5 are represented in Figure 3.16, which visually shows a comparison of the fiber-measured crack growth and the true crack growth. For both resolutions, the fiber-measured crack growth is within ± 3 mm from the true crack growth with the majority being within ± 2 mm. Similar results were found from the additional three specimens as reported in Appendix C.

The fiber-measured crack growth can also be used to map the shape of the crack front. Figure 3.17 shows the mapping of the crack front shape determined from the optical fibers; these results are overlaid onto a photo of the ENF specimens with the true crack fronts shown in silver. Figure 3.17d shows two fiber passes because the fiber in specimen ENF-104 broke before the third pass. The fiber-measured crack fronts compare well with the true crack growth data.

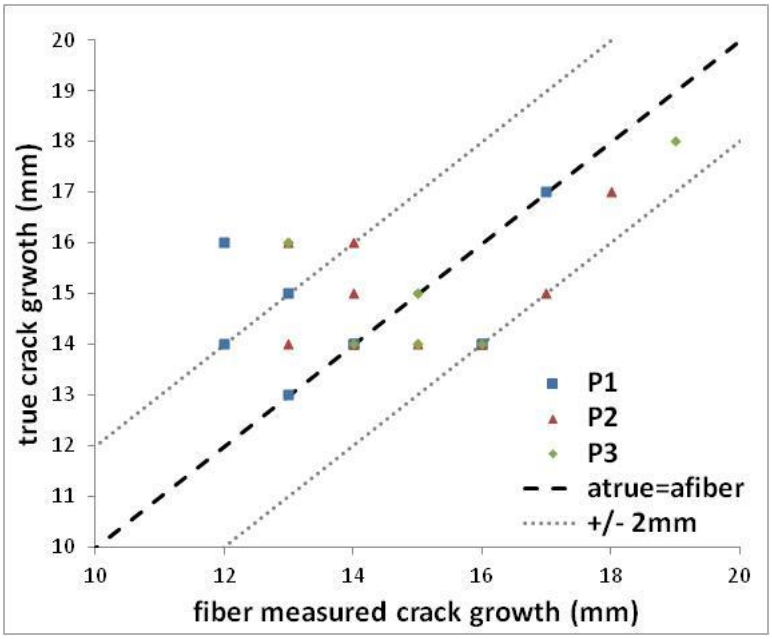

(a)

Figure 3.16 Comparison of true and fiber measured crack growth for specimen ENF-101 with (a) 3 mm gauge length and 3 mm spacing and (b) 3 mm gauge length and 1 mm spacing

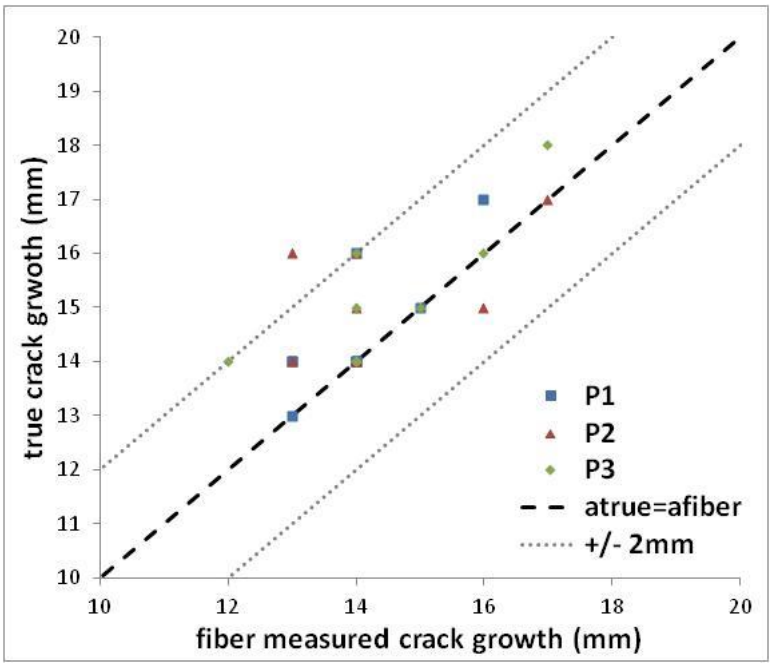

(b)

Figure 3.16 (continued)

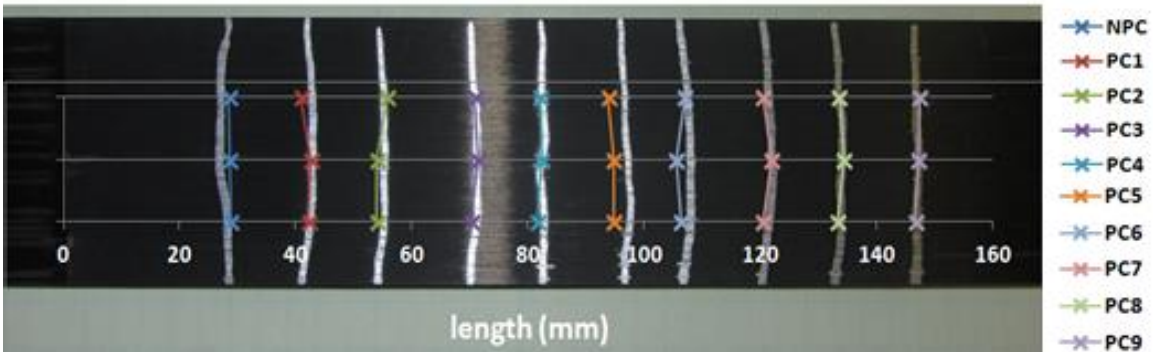

(a)

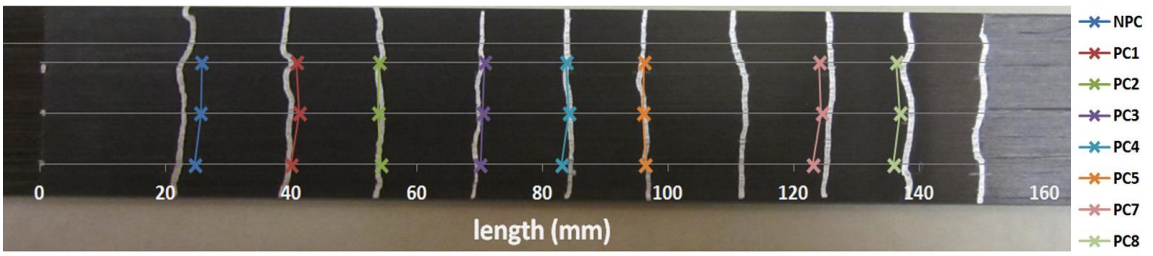

(b)

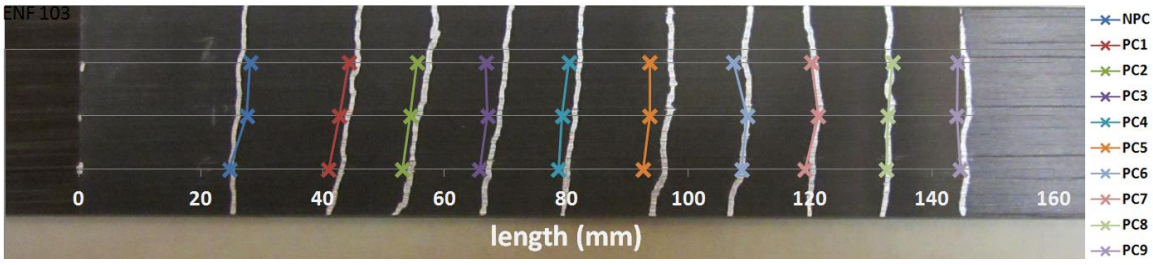

(c)

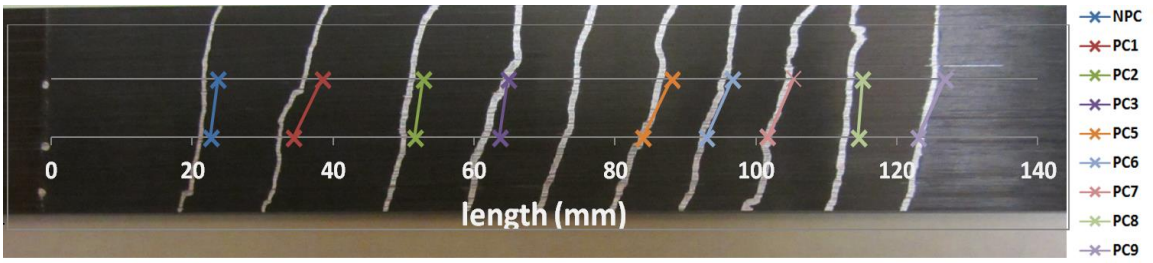

(d)

Figure 3.17 Crack front shape determined from optical fiber for (a) ENF-101, (b) ENF-102, (c) ENF 103, (d) ENF-104

CHAPTER IV

CONCLUSIONS

The strain distributions in the DLS and ENF specimens were successfully obtained through embedded distributed optical sensors. Because of the fragile nature of the optical fibers, special care was taken during both the manufacturing and testing processes. A manufacturing process was for embedding optical fibers was developed; this can be utilized for future specimen fabrication. Specimens with and without optical fibers were tested to show that the embedded fibers do not affect adhesive bond strength when loaded in tension or the mode II fracture toughness values for unidirectional composite laminates. The strain profiles obtained from the optical fibers correlated well with results from FE models for both the DLS specimens and the ENF specimens. The strain distributions obtained from the optical fibers in the ENF specimen's were used to find the amount of mode II delamination growth that occurred during ENF tests and map the location and shape of the delamination front.

4.1 Limitations

Although optical fibers have many attributes, they are also fragile and must be handled very carefully during fabrication and testing. Additionally, data during specimen failure in the DLS and ENF testing could not be collected since the LUNA ODiSI A system has a very low sampling rate (1 Hz). Therefore, strain profiles were collected only before and after the events of interest, and the changes in the strain during failure events

could not be observed. Also, the exact location of specific strain measurements can be difficult to locate precisely along the fiber. For this study, measurements were located based on known reference points such as the ingress/egress points where the fiber enters/exits the specimen. However, since strains are averaged over specified optical fiber the gauge length, the point of interest could lie anywhere within that length; since other locations are measured from that data point, the strain data could be off up to a gauge length. This causes some small uncertainty in the location of measurements when comparing parallel fiber paths. Therefore, a smaller gauge length results in a more accurate location of the strain data, but with increased processing time.

4.2 Ongoing and Future Work

These case studies employed a method for embedding optical fibers and processing data. Further studies should be performed to further characterization of the adhesive bonds. In this study, catastrophic failures were observed, instead of studying damage growth in the adhesive. Observing a slower, controlled failure could lead to a system to detect and characterize adhesive damage. Ongoing work includes embedding optical fibers in double cantilever beam test specimens to map the crack front for Mode I delaminations (similar to the ENF tests) and in specimens subjected to low velocity impacts to characterize delamination damage.

REFERENCES

[1] Culshaw, B. and A. Kersey. Fiber-optic sensing: A historical perspective. IEEE/OSA J. Lightw. Tech.2008, 26, 1064-1078.

[2] Guo, H., G. Xiao, N. Mrad, and J. Yao. "Fiber Optic Sensors for Structural Health Monitoring of Air Platforms."*Sensors* 11.12 (2011): 3687-705.

[3] Grave, J., M. Håheim, and A. Echtermeyer. "Measuring Changing Strain Fields in Composites with Distributed Fiber-Optic Sensing Using the Optical Backscatter Reflectometer." *Composites Part B: Engineering* 74 (2015): 138-46.

[4] Murayama, H., K. Kageyama, K. Uzawa, K. Ohara, and H. Igawa. "Strain Monitoring of a Single-lap Joint with Embedded Fiber-optic Distributed Sensors." *Structural Health Monitoring* 11.3 (2011): 325-44.

[5] Meadows, L., R. Sullivan, and K. Vehorn. "Distributed Optical Sensing in Composite Laminate Adhesive Bonds." Proc. of American Institute of Aeronautics and Astronautics SciTech 4-8 January 2016, San Diego, CA.

[6] Meadows, L., R. Sullivan, V.Ranatunga, K. Vehorn, K. Brown, and S. Olson. "Distributed Optical Sensing in Composite Laminate End-Notched Flexure Tests." Proc. of 31st American Society for Composites Technical Conference 19-21 September 2016, Williamsburg, VA.

[7] Glisic, B., and D. Inaudi. Fibre optic methods for structural health monitoring. John Wiley & Sons, 2008.

[8] Grattan, S., S. Taylor, P. Basheer, T. Sun, and K. Grattan, “Structural Health Monitoring – Better Solutions Using Fiber Optic Sensors?,” Proceedings of the IEEE Sensors 2009 Conference, p. 811-814, October 25-28, 2009.

[9] Li, H., D. Li, and G. Song. "Recent applications of fiber optic sensors to health monitoring in civil engineering." *Engineering Structures* 26.11 (2004): 1647-1657.

[10] Kressel, I., A. Handelman, Y. Botsev, J. Balter, P. Guedj, N. Gorbatov, M. Tur, A. Pillai, M. Prasad, N. Gupta, A. Joseph, and R. Sundaram, “Evaluation of Flight Data from an Airworthy Structural Health Monitoring System Integrally Embedded in an Unmanned Air Vehicle,” presented at the 6th European Workshop on Structural Health Monitoring, Dresden, Germany, July 3-6, 2012.

[11] Pedrazzani, J., S. Klute, D. Gifford, A. Sang, and M. Froggatt, "Embedded and Surface Mounted Fiber Optic Sensors Detect Manufacturing Defects and Accumulated Damage as a Wind Turbine Blade is Cycled to Failure," Proceedings of the 2012 SAMPE International Symposium and Exhibition – Emerging Opportunities: Materials and Process Solutions, Baltimore, MD, May 21-24, 2012.

[12] Razali, N., M. Abu Bakar, N. Tamchek, M. Yaacob, A. Latif, K. Zakaria, and M. Mahdi. "Fiber Bragg Grating for Pressure Monitoring of Full Composite Lightweight Epoxy Sleeve Strengthening System for Submarine Pipeline." Journal *of Natural Gas Science and Engineering* 26 (2015): 135-41

[13] Park, C., et al. "Bird strike event monitoring in a composite UAV wing using high speed optical fiber sensing system." *Composites Science and Technology* 72.4 (2012): 498-505.

[14] Canal, L., R. Sarfaraz, G.Violakis, J. Botsis, V. Michaud, and H. Limberger. "Monitoring Strain Gradients in Adhesive Composite Joints by Embedded Fiber Bragg Grating Sensors." *Composite Structures* 112 (2014): 241-47.

[15] Capell, T., J. Palaniappan, S. Ogin, A. Crocombe, G. Reed, A. Thorne, L. Mohanty, and S. Tjin. "The Use of an Embedded Chirped Fibre Bragg Grating Sensor to Monitor Disbond Initiation and Growth in Adhesively Bonded Composite/metal Single Lap Joints." *Journal of Optics A: Pure and Applied Optics J. Opt. A: Pure Appl. Opt.* 9.6 (2007)

[16] Ling, H., K. Lau, Z. Su, and E.Wong. "Monitoring Mode II Fracture Behavior of Composite Laminates Using Embedded Fiber-optic Sensors." *Composites Part B: Engineering* 38.4 (2007): 488-97.

[17] Sanderson, A., S. Ogin, A. Crocombe, M. Gower, R. Lee, S. Tijn, and B. Lin. "Monitoring Crack Growth in a DCB Test Using a Surface-Bonded Chirped FBG Sensor." Proc. of 18th International Conference on Composite Materials.

[18] Bernasconi, A., M. Carboni, and L. Comolli. "Monitoring of Fatigue Crack Growth in Composite Adhesively Bonded Joints Using Fiber Bragg Gratings." *Procedia Engineering* 10 (2011): 207-12.

[19] Güemes, A., A. Fernandez-Lopez, and A. Lozano. "Fiber Optic Distributed Sensing."

[20] Wild, G. and S. Hinckley, "Distributed Optical Fibre Smart Sensors for Structural Health Monitoring: A Smart Transducer Interface Module," Proceedings of the 5th International Conference on Intelligent Sensors, Sensor Networks and Information Processing (ISSNIP), p. 373-378, Melbourne, Australia, December 7-10, 2009.

[21] Samiec, D. "Distributed Fiber-optic Temperature and Strain Measurement with Extremely High Spatial Resolution." *Photonik International*, June 2011.

[22] Luna. 01 Aug. 2012. Web. <http://lunainc.com/>.

[23] ASTM Standard D 3528, 1996 (2008), "Standard Test Method for Strength Properties of Double Lap Shear Adhesive Joints by Tension Loading," ASTM International, West Conshohocken, PA.

[24] Ranatunga, V., and S. Clay. "Cohesive Modeling of Damage Growth in Z-pinned Laminates under Mode-I Loading." *Journal of Composite Materials* 47.26 (2012): 3269-283.

[25] Guess, T., E. Reedy, and M. Stavig. "Mechanical Properties of Hysol EA-9394 Structural Adhesive." *Sandia Report* (1995)

[26] Instron. Illinois Tool Works Inc., Web. <http://www.instron.us/.

[27] Abaqus. Dassault Systèmes. Web. <http://www.3ds.com/products-services/simulia/products/abaqus/>.

[28] ASTM Standard D 7905, 2014, "Standard Test Method for Determination of the Mode II Interlaminar Fracture Toughness of Unidirectional Fiber-Reinforced Polymer Matrix Composites," ASTM International, West Conshohocken, PA.

[29] Ranatunga, V., and S. Clay. "Cohesive Modeling of Damage Growth in Z-pinned Laminates under Mode-I Loading." *Journal of Composite Materials* 47.26 (2012): 3269-283.

[30] Instru-Met Corporation.Web. <http://www.instrumet.com/>

[31] Ranatunga, V., and S. Clay, “Testing and Analysis of the End-Notched Flexure Specimen for Composites under Mode-II Fracture.” Air Force Research Laboratory.

[32] Shivakumar, K., and A. Bhargava. "Failure Mechanics of a Composite Laminate Embedded with a Fiber Optic Sensor." *Journal of Composite Materials* 39.9 (2005): 777-98.

[33] MATLAB R2015b. The MathWorks Inc., Natick, MA, 2015.

APPENDIX A

ADDITONAL DOUBLE LAP SHEAR DATA

The DLS data in section 2.2.2 is data for specimen Fiber3 from the panel fabricated DLS specimens. The optical fiber data from the remaining specimens, Fiber1 and Fiber2, from this panel was unusable perhaps due to bad baseline data. The data shown in the following sections is from specimens fabricated individually for preliminary testing. The strain data shows additional examples of the ingress/egress points, butt joint, and bowl shaped distribution as expected; however, the failure loads varied due to inconsistent bond line thickness.

A.1 DLS-P1

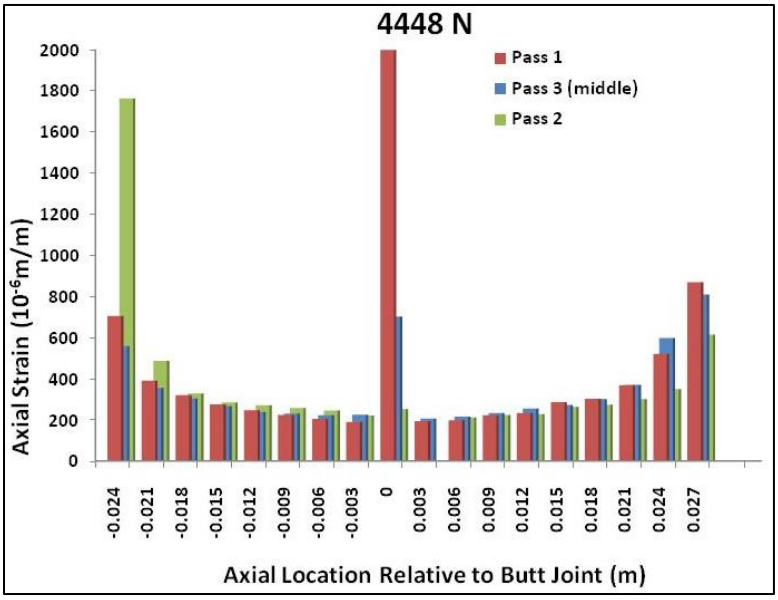

(a)

Figure A.1 DLS-P1 strain distributions at (a) 4448 N, (b) 8896 N, (c) 13,345 N, and (b) 21,676 N (near failure)

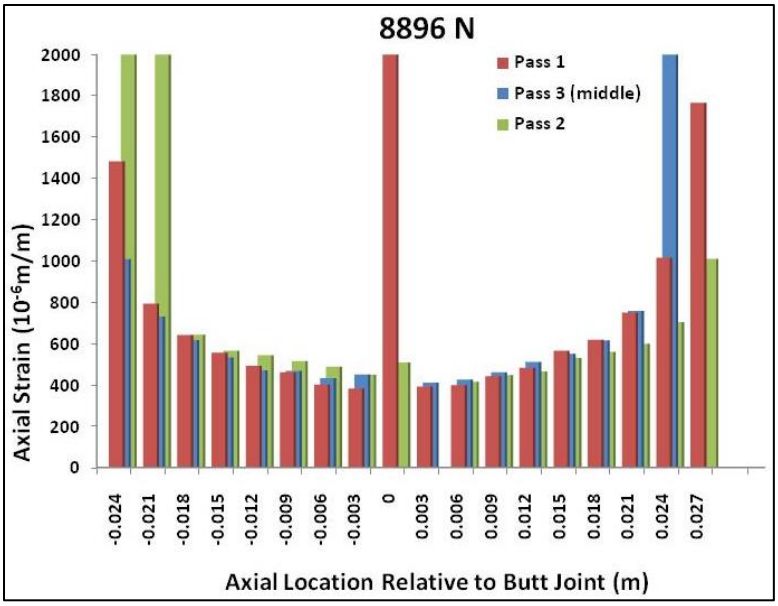

(b)

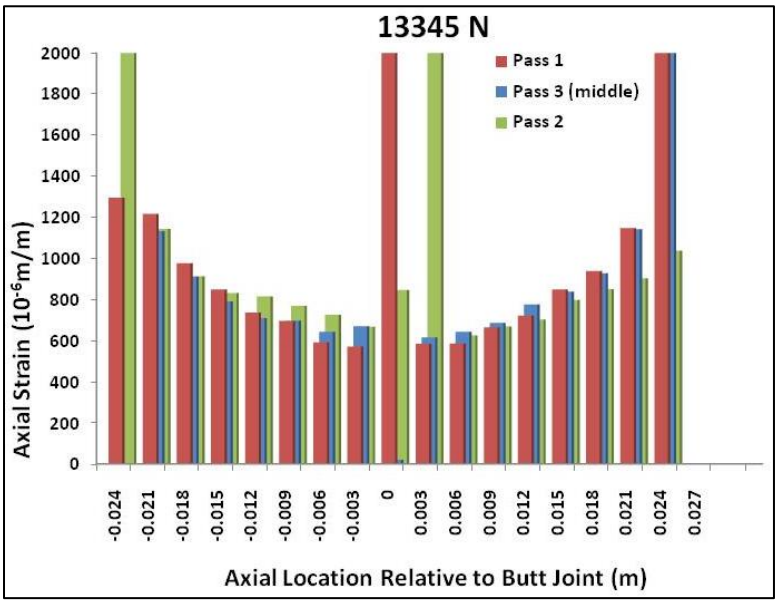

(c)

Figure A.1 (continued)

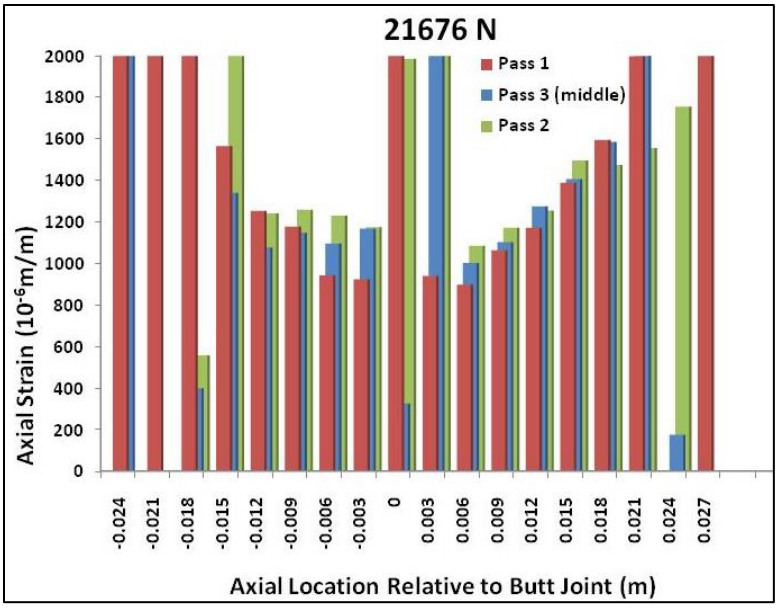

(d)

Figure A.1 (continued)

A.2 DLS-P2

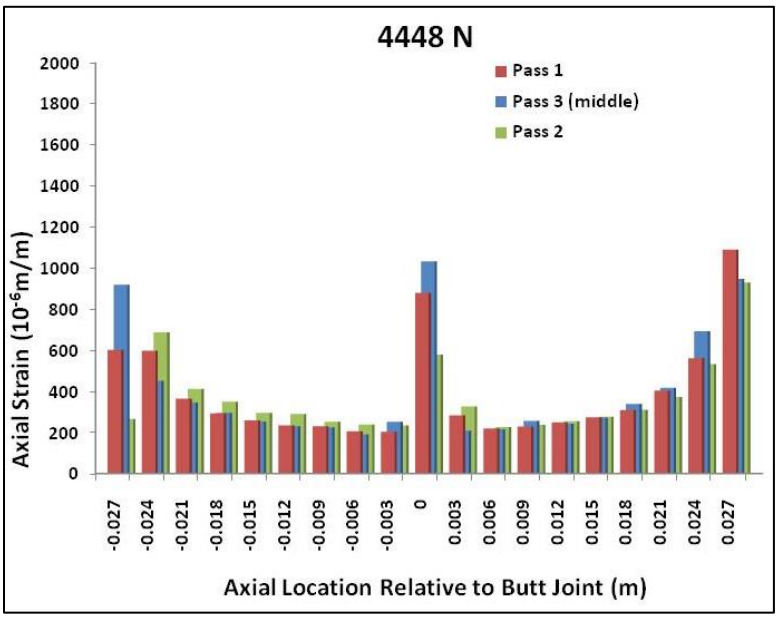

(a)

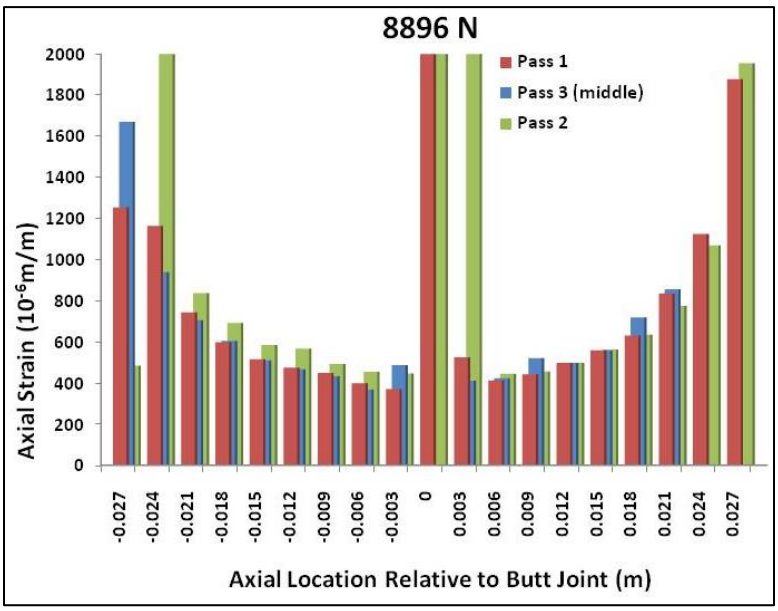

(b)

Figure A.2 DLS-P2 strain distributions at (a) 4448 N, (b) 8896 N, (c) 13,345 N, and (b) 18,892 N (near failure)

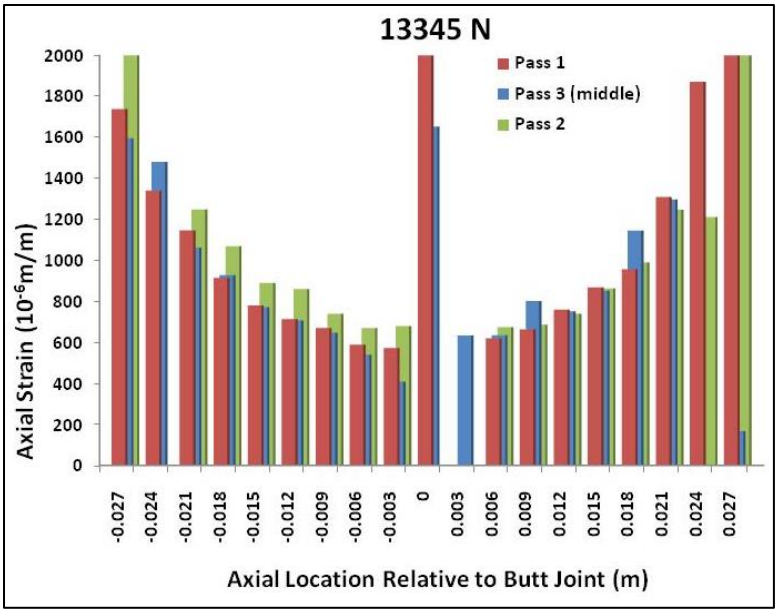

(c)

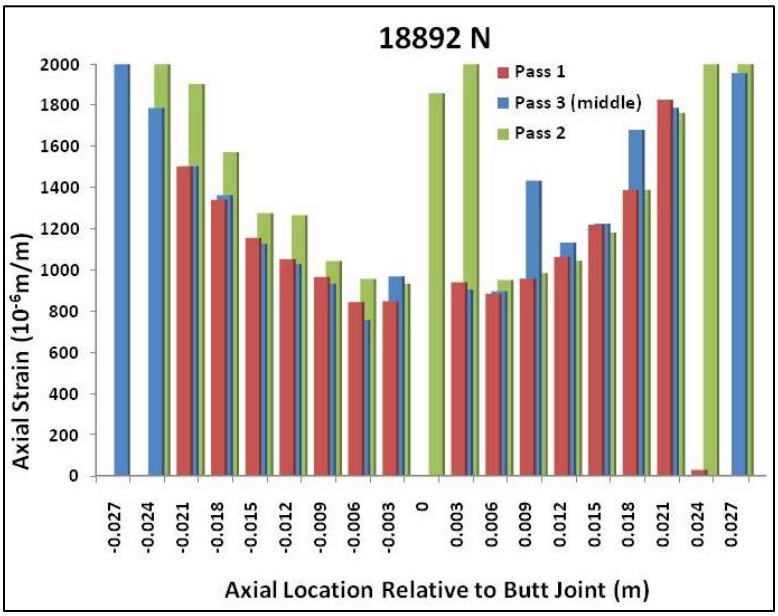

(d)

Figure A.2 (continued)

APPENDIX B

ADDITOINAL ENF STRAIN DATA

B.1 ENF-101 Strain Data

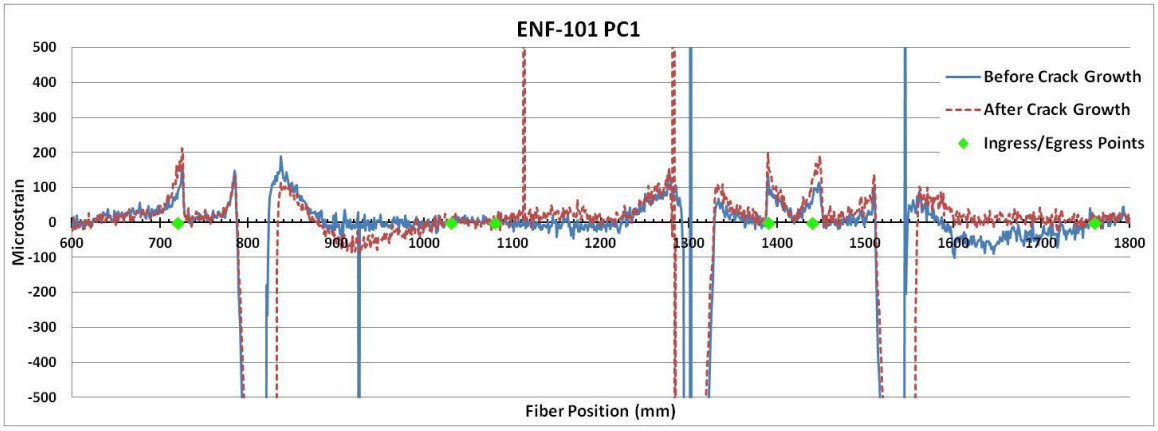

Figure B.1 ENF-101 PC1 strain data before and after crack growth

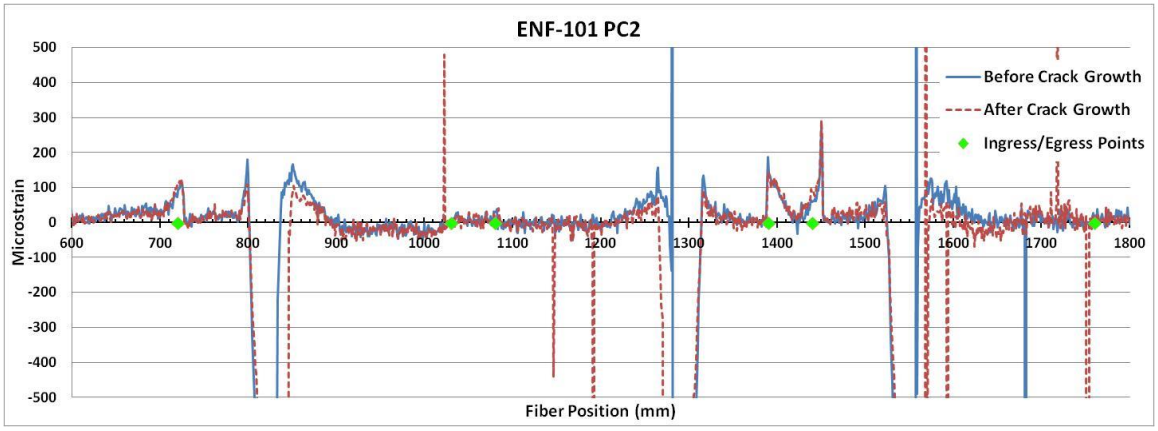

Figure B.2 ENF-101 PC2 strain data before and after crack growth

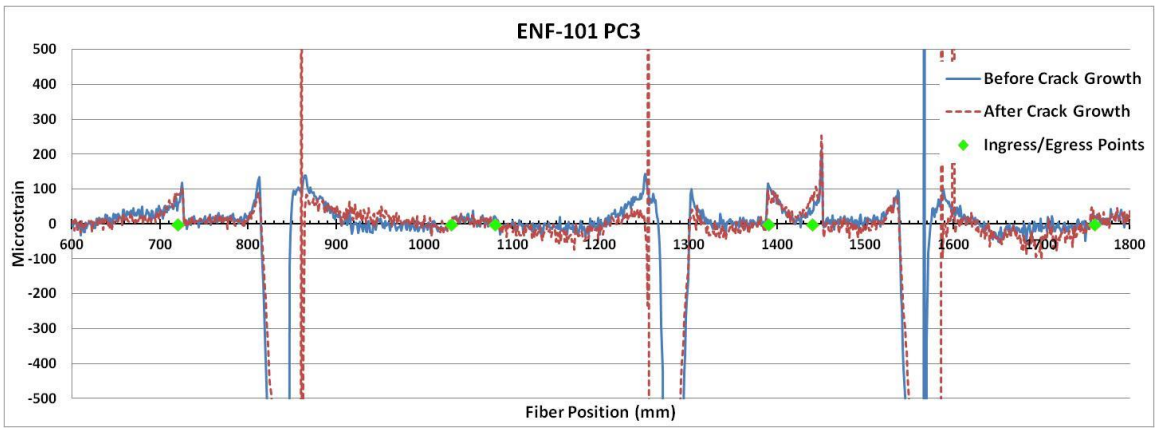

Figure B.3 ENF-101 PC3 strain data before and after crack growth

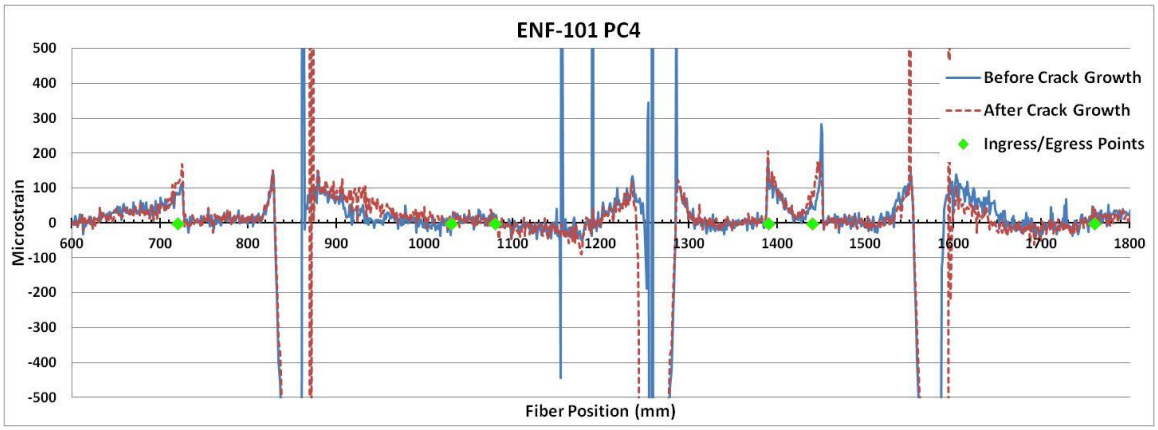

Figure B.4 ENF-101 PC4 strain data before and after crack growth

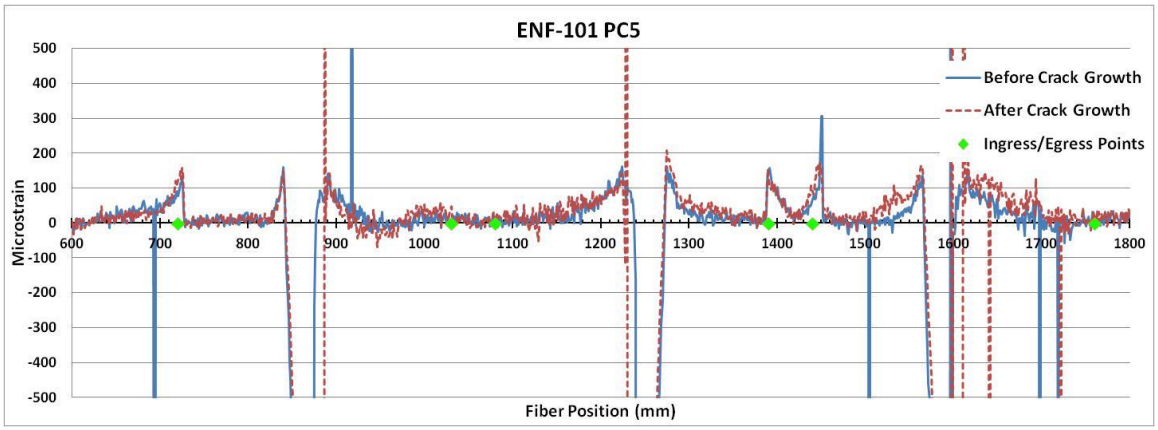

Figure B.5 ENF-101 PC5 strain data before and after crack growth

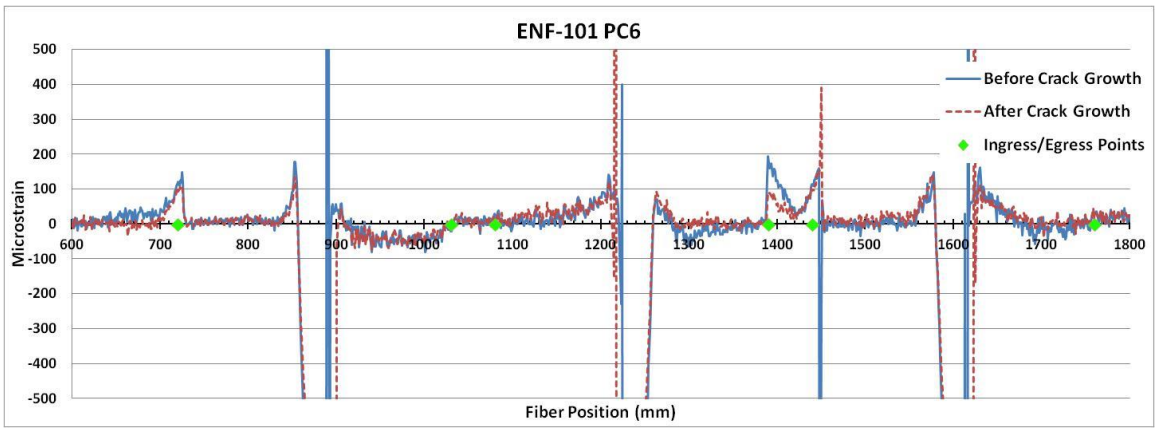

Figure B.6 ENF-101 PC6 strain data before and after crack growth

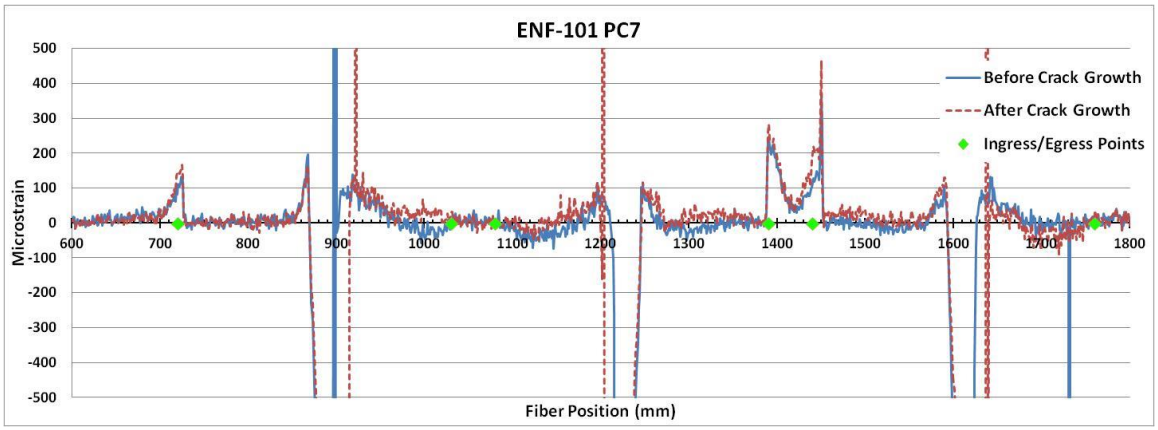

Figure B.7 ENF-101 PC7 strain data before and after crack growth

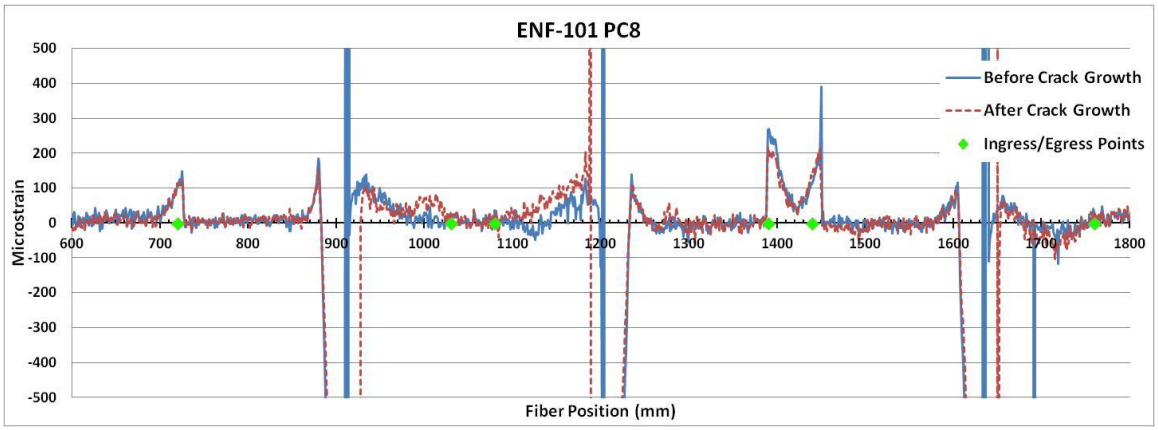

Figure B.8 ENF-101 PC8 strain data before and after crack growth

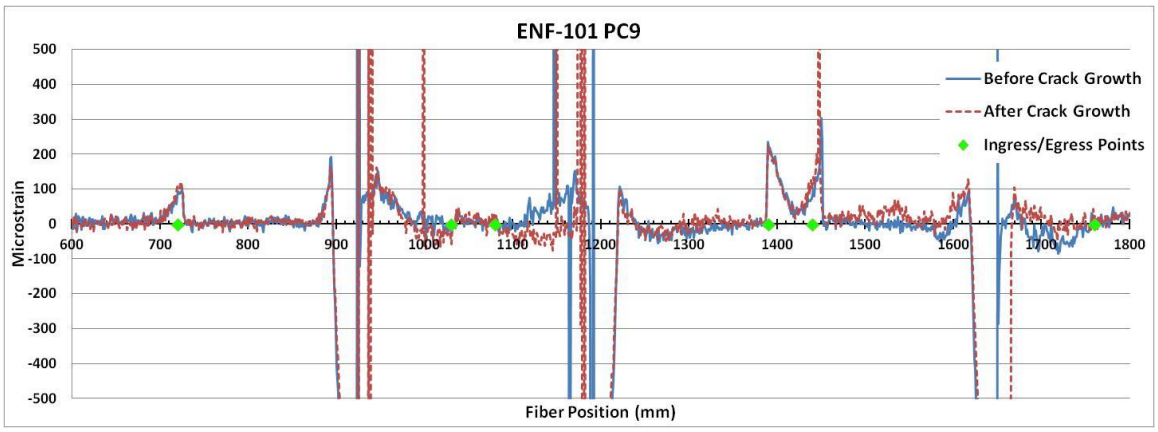

Figure B.9 ENF-101 PC9 strain data before and after crack growth

B.2 ENF-102 Strain Data

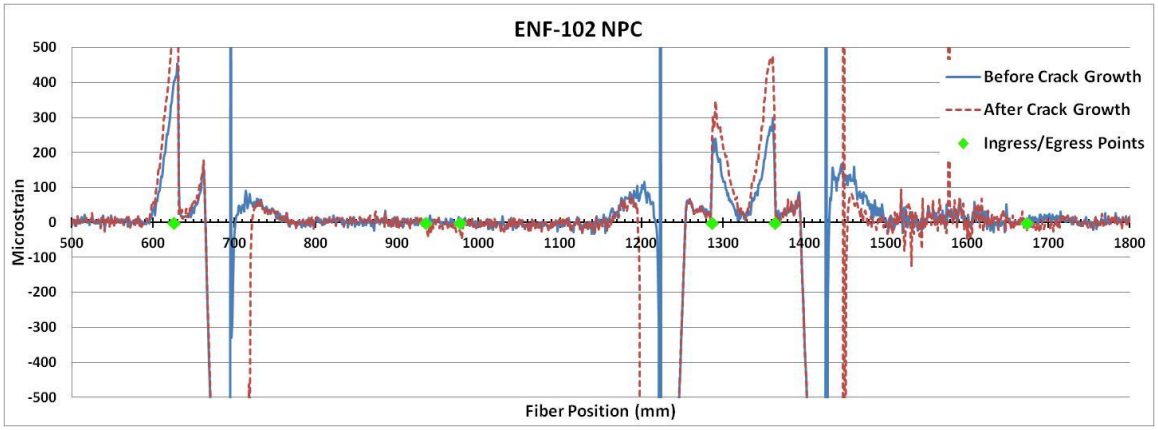

Figure B.10 ENF-102 NPC strain data before and after crack growth

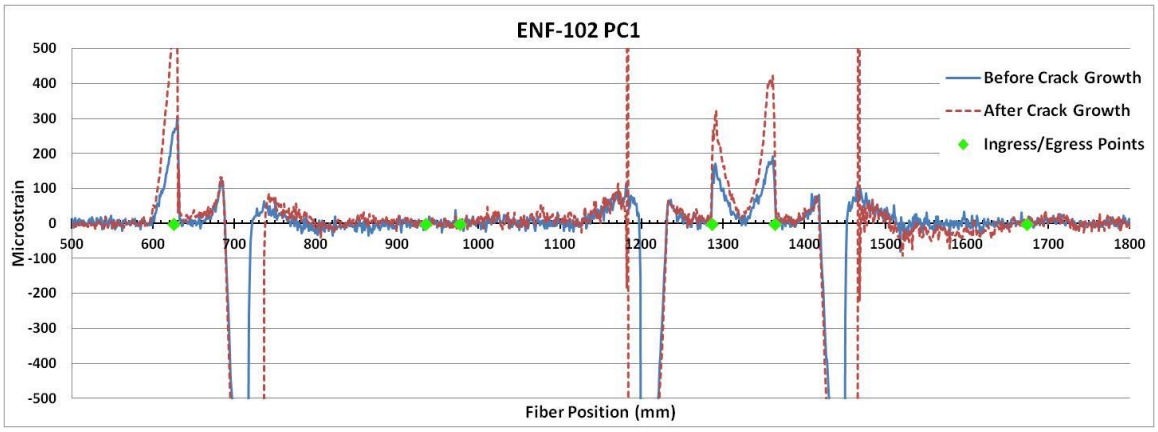

Figure B.11 ENF-102 PC1 strain data before and after crack growth

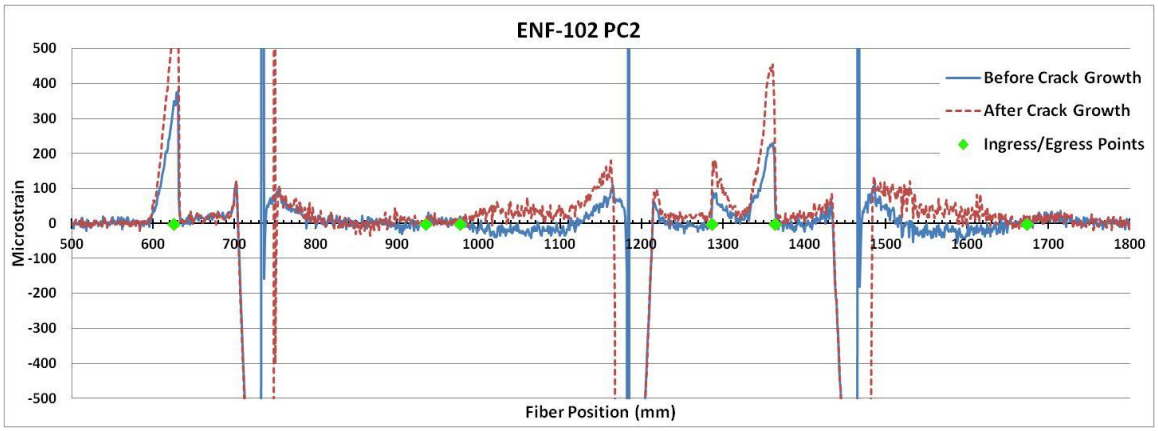

Figure B.12 ENF-102 PC2 strain data before and after crack growth

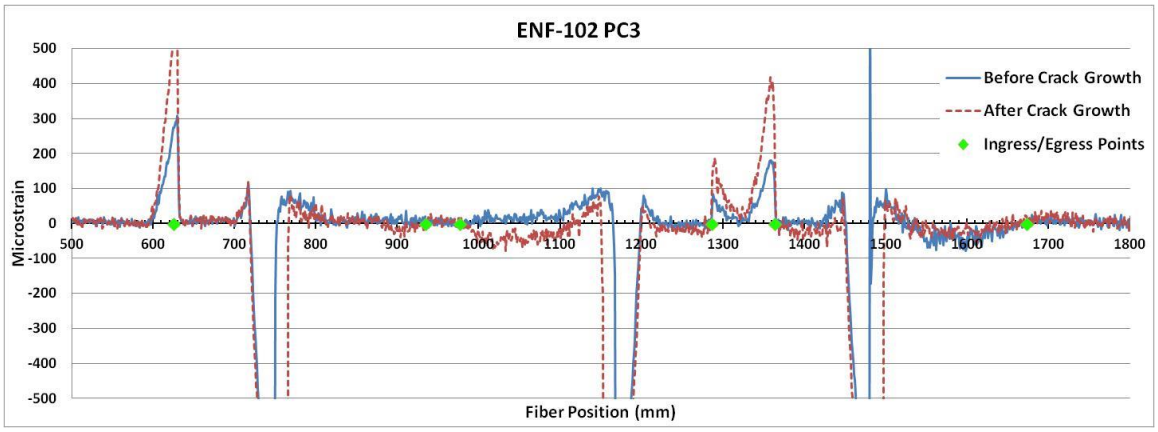

Figure B.13 ENF-102 PC3 strain data before and after crack growth

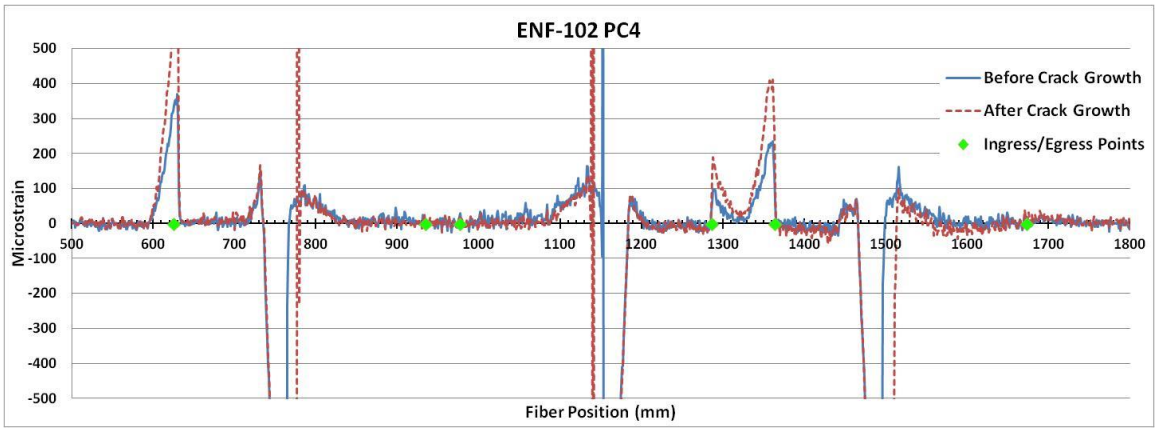

Figure B.14 ENF-102 PC4 strain data before and after crack growth

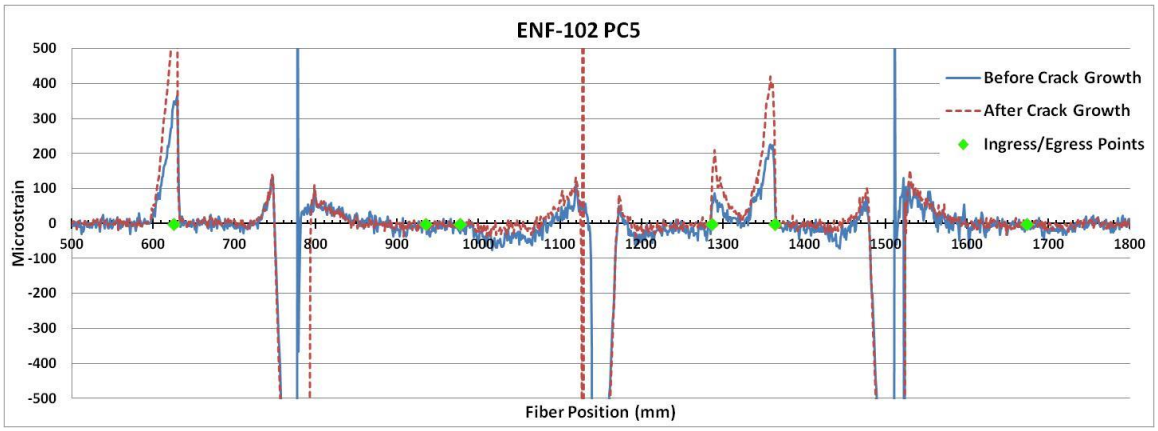

Figure B.15 ENF-102 PC5 strain data before and after crack growth

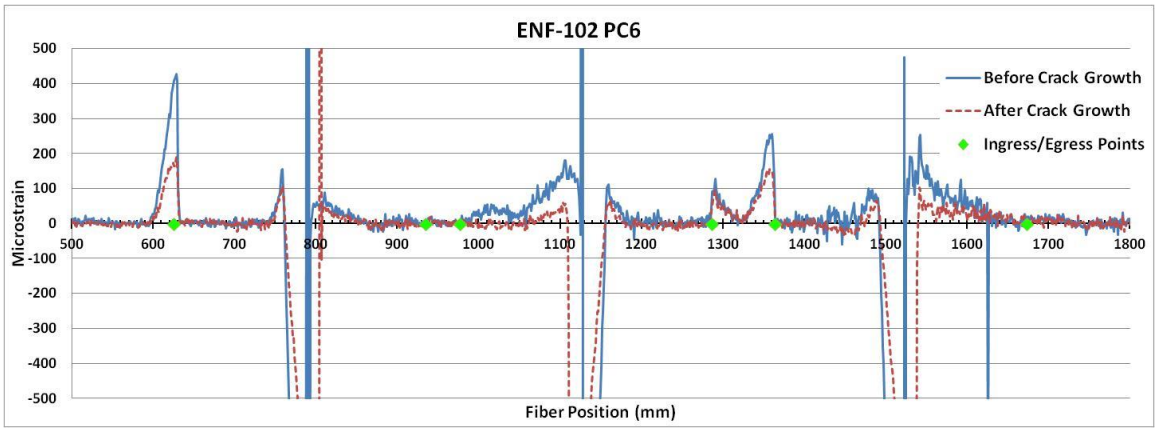

Figure B.16 ENF-102 PC6 strain data before and after crack growth

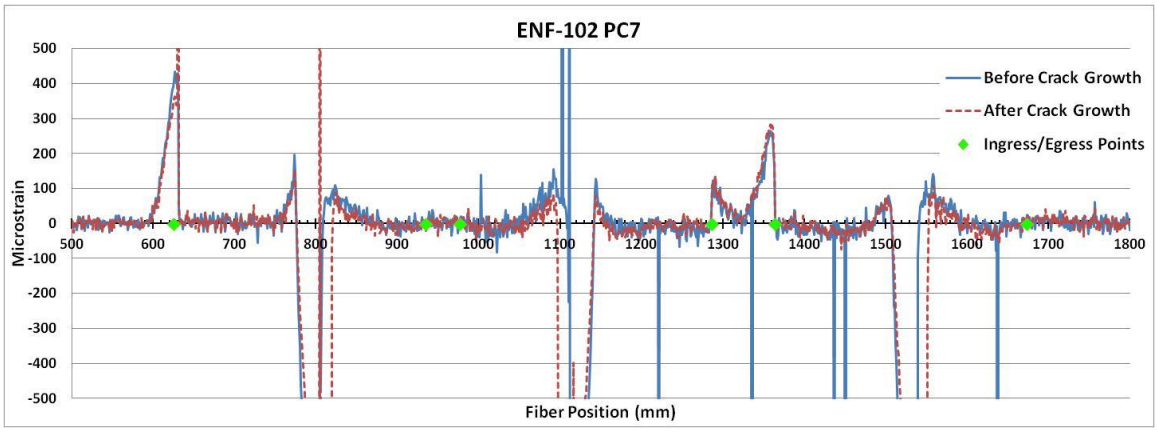

Figure B.17 ENF-102 PC7 strain data before and after crack growth

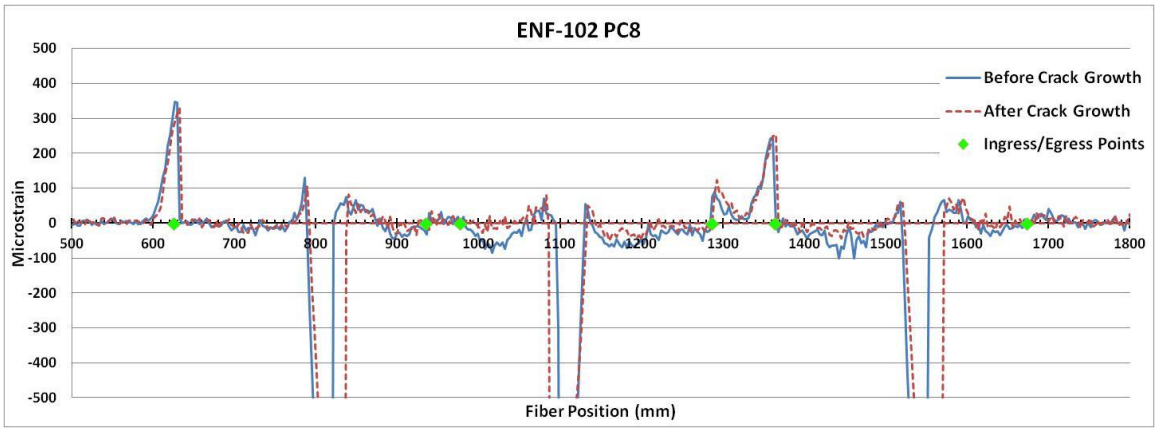

Figure B.18 ENF-102 PC8 strain data before and after crack growth

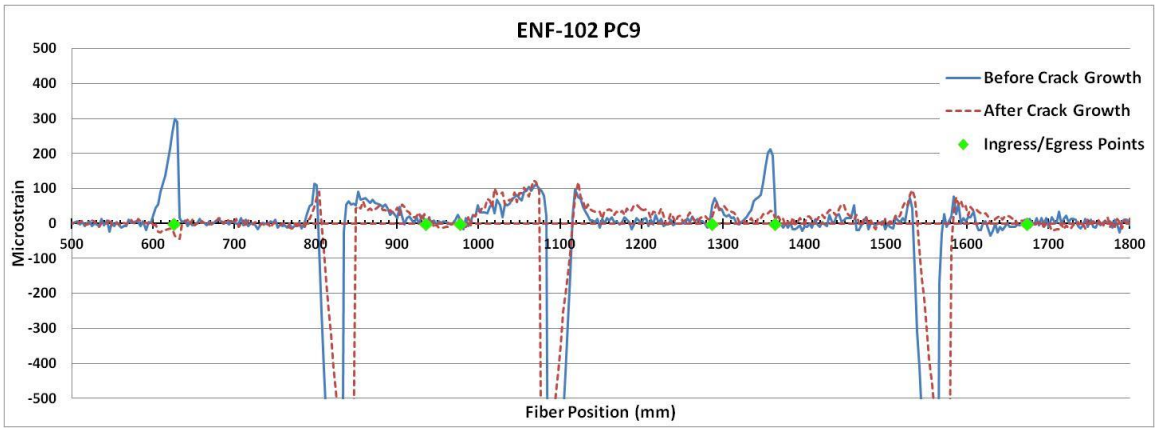

Figure B.19 ENF-102 PC9 strain data before and after crack growth

B.3 ENF-103 Strain Data

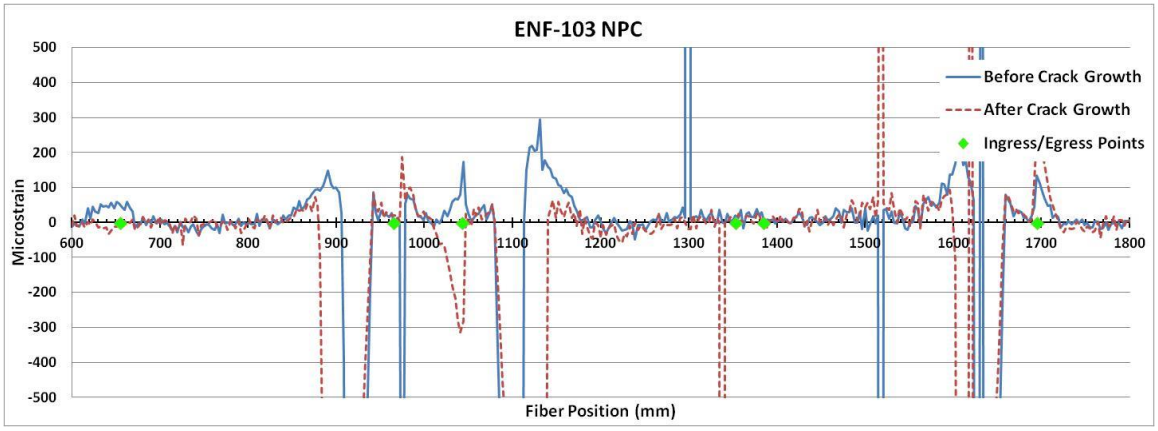

Figure B.20 ENF-103 NPC strain data before and after crack growth

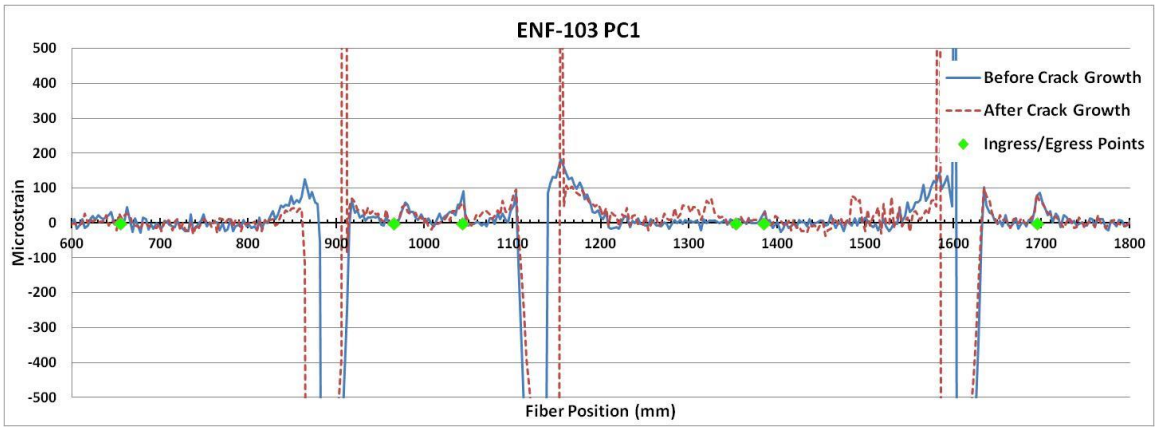

Figure B.21 ENF-103 PC1 strain data before and after crack growth

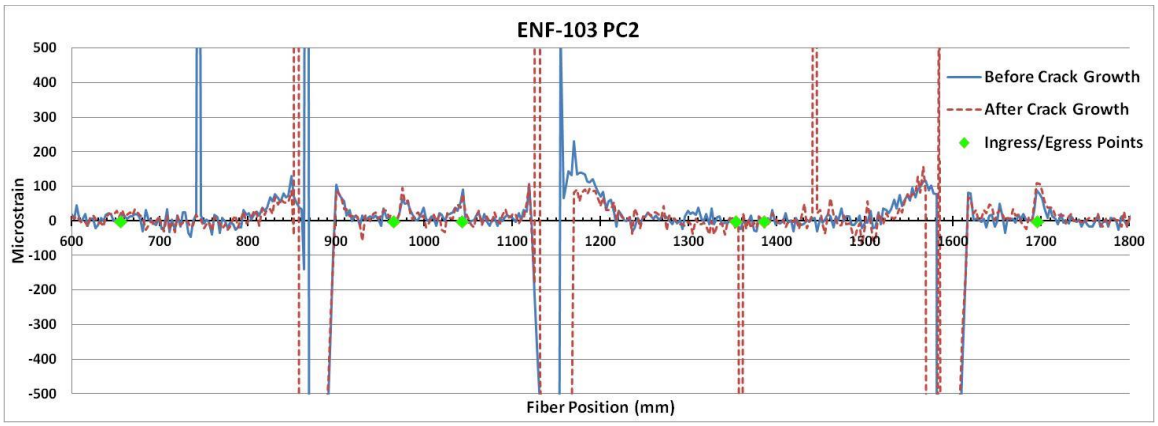

Figure B.22 ENF-103 PC2 strain data before and after crack growth

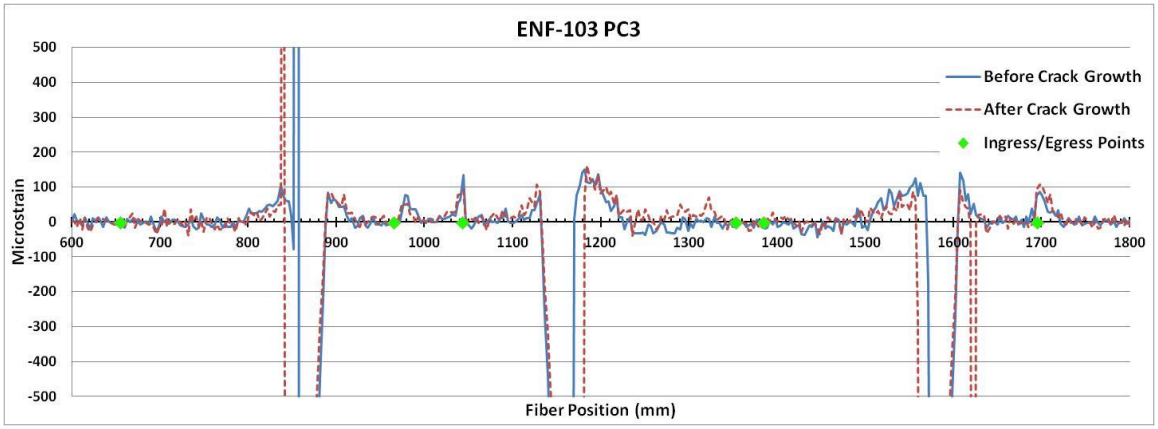

Figure B.23 ENF-103 PC3 strain data before and after crack growth

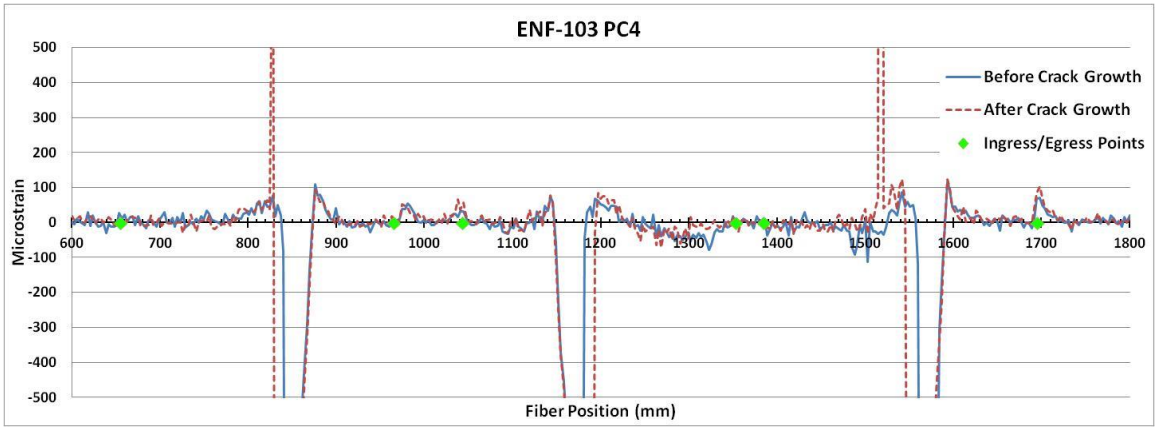

Figure B.24 ENF-103 PC4 strain data before and after crack growth

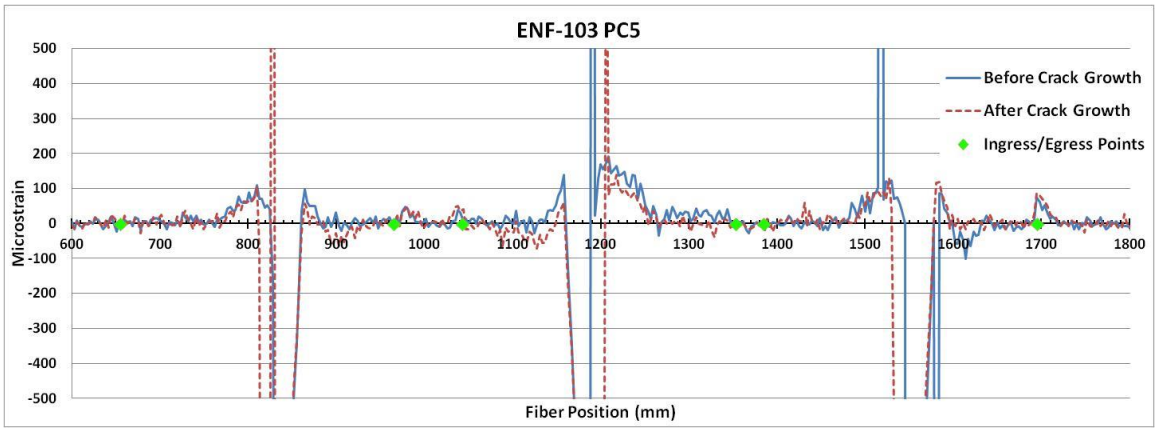

Figure B.25 ENF-103 PC5 strain data before and after crack growth

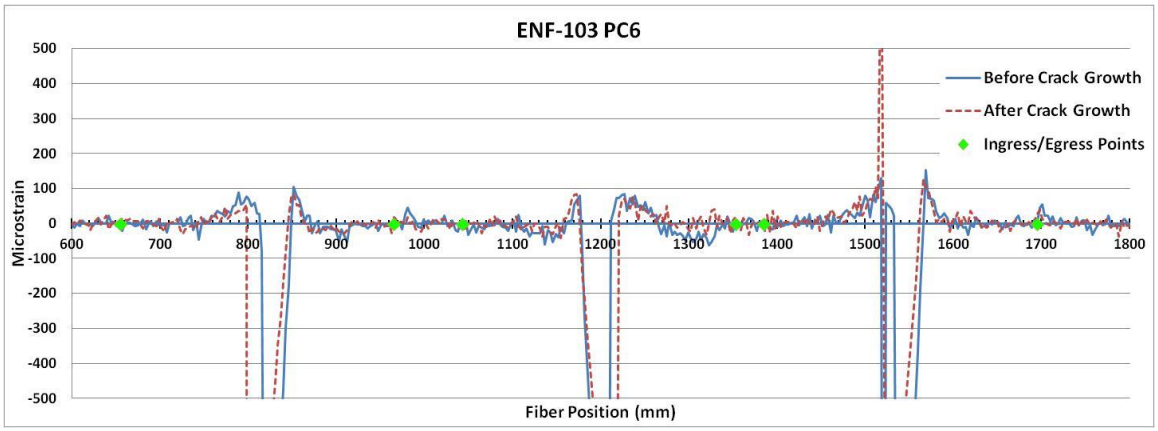

Figure B.26 ENF-103 PC6 strain data before and after crack growth

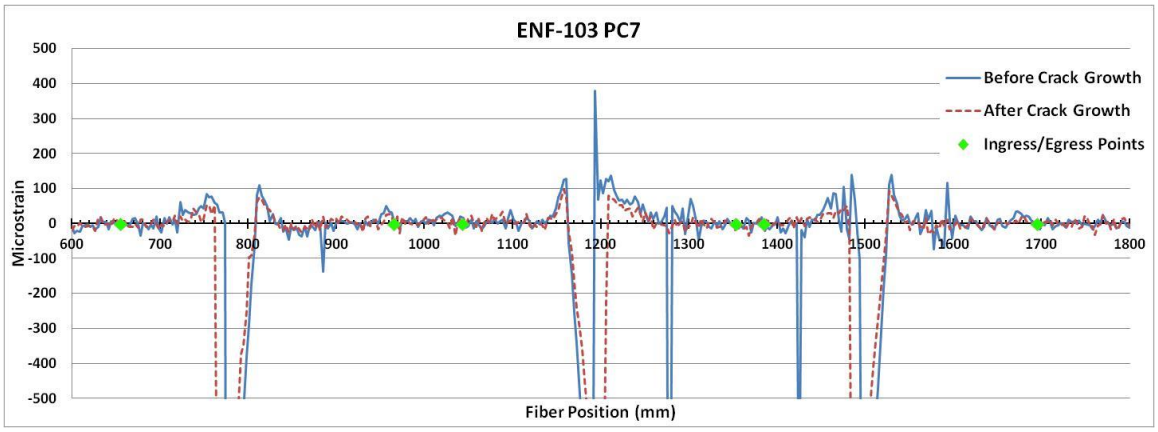

Figure B.27 ENF-103 PC7 strain data before and after crack growth

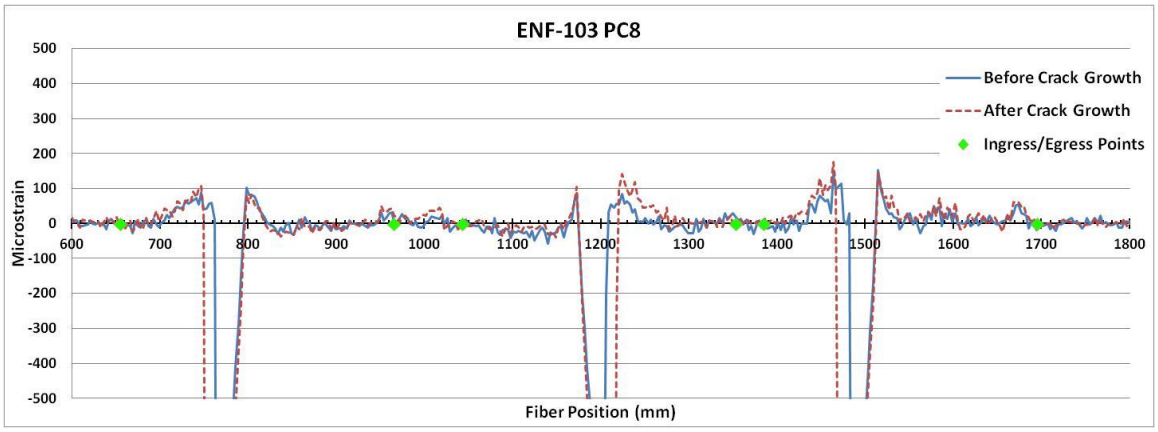

Figure B.28 ENF-103 PC8 strain data before and after crack growth

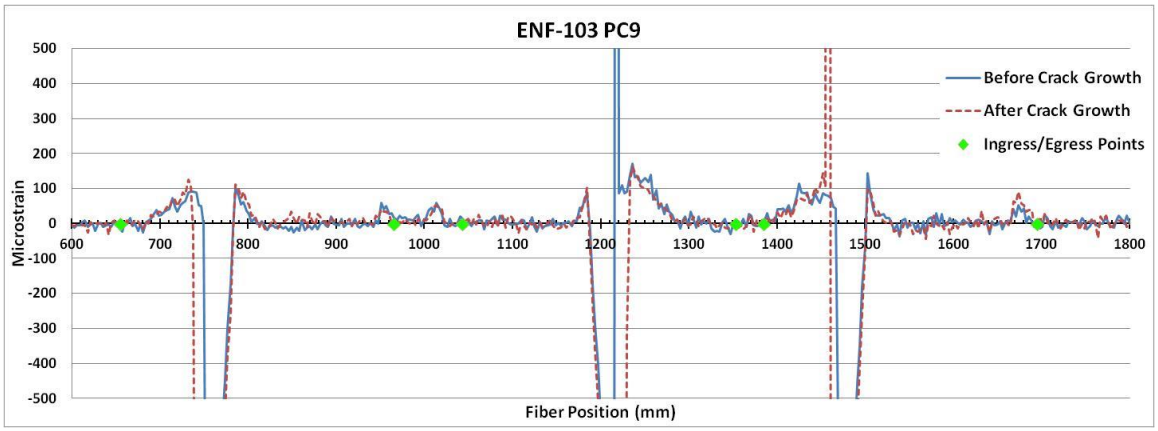

Figure B.29 ENF-103 PC9 strain data before and after crack growth

B.4 ENF-104 Strain Data

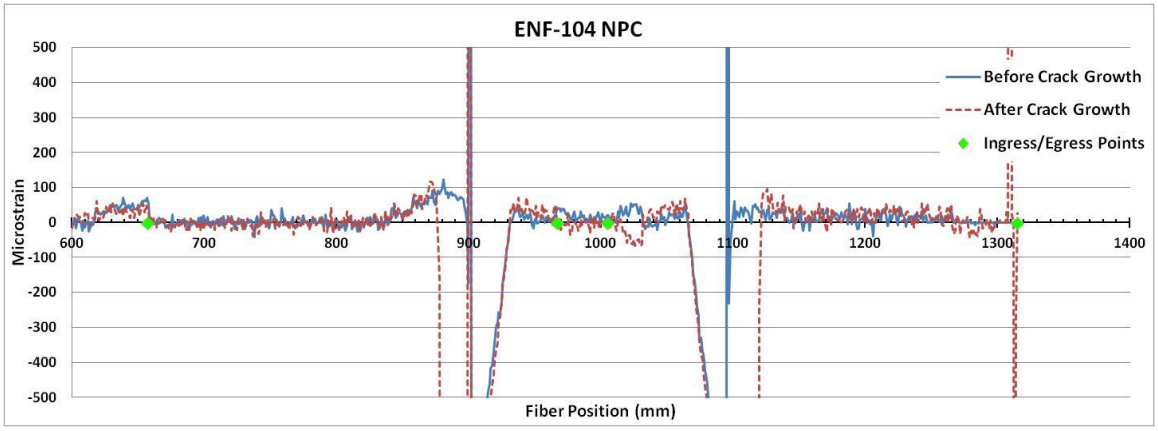

Figure B.30 ENF-104 NPC strain data before and after crack growth

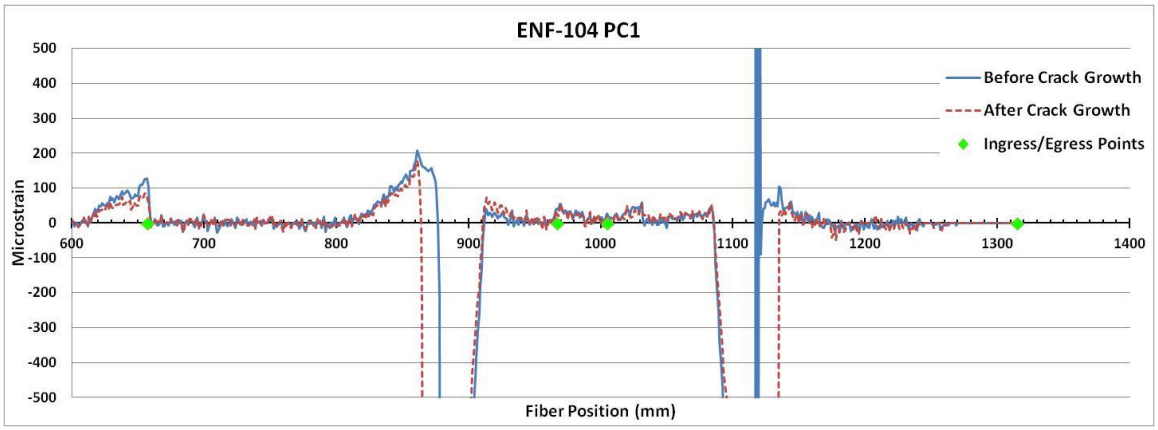

Figure B.31 ENF-104 PC1 strain data before and after crack growth

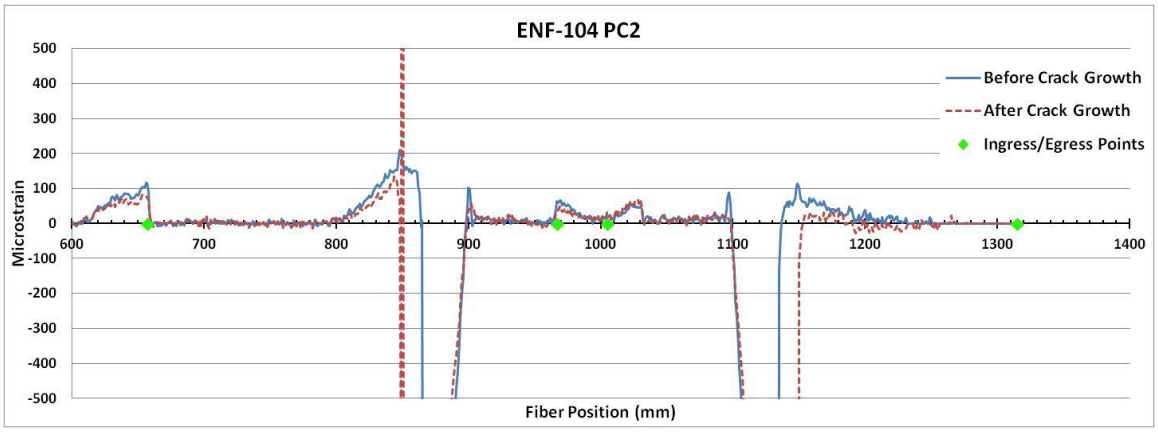

Figure B.32 ENF-104 PC2 strain data before and after crack growth

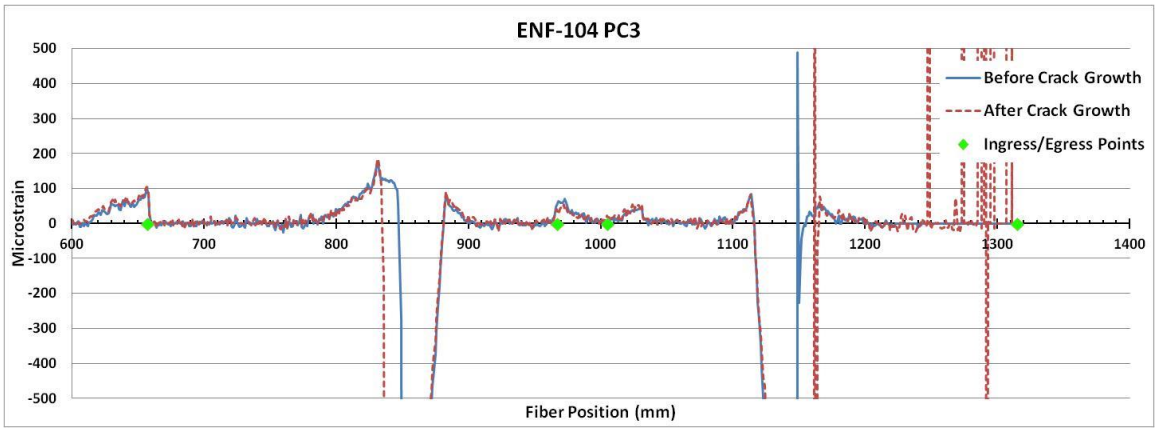

Figure B.33 ENF-104 PC3 strain data before and after crack growth

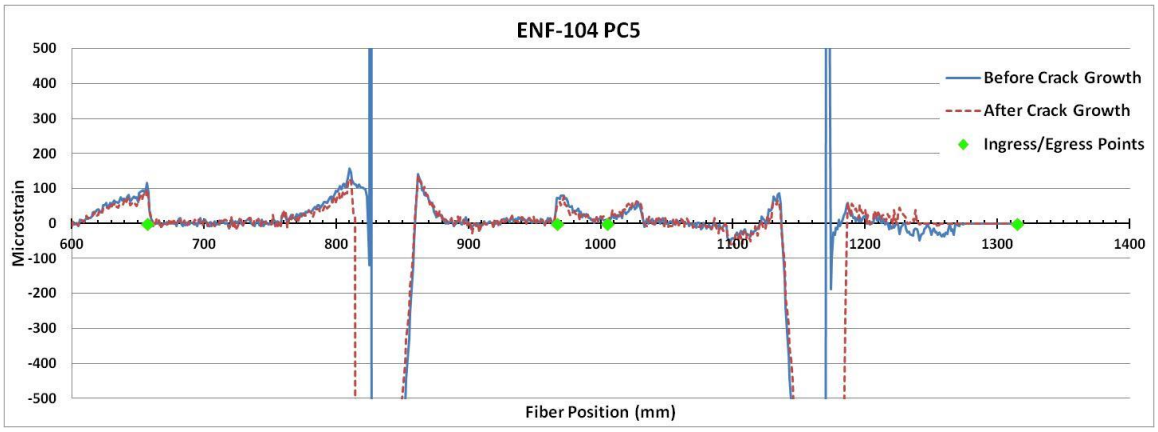

Figure B.34 ENF-104 PC5 strain data before and after crack growth

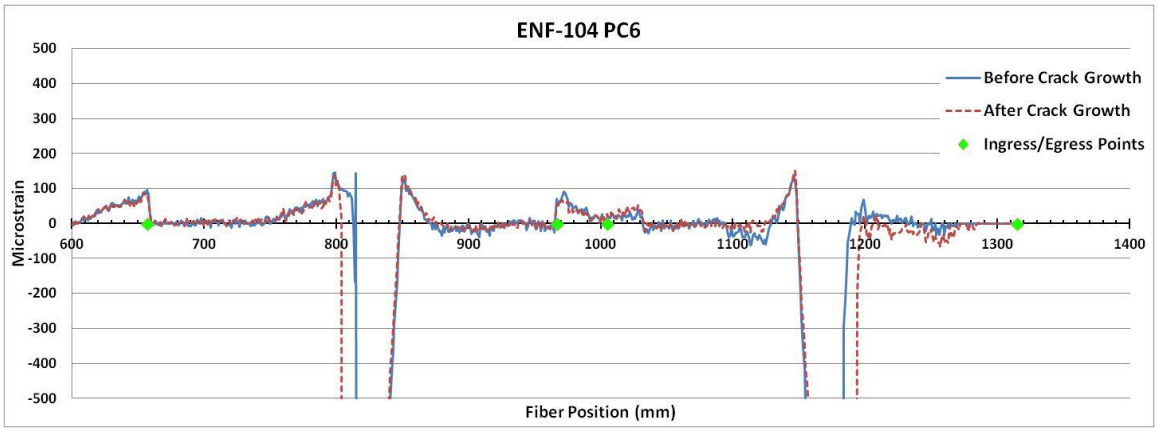

Figure B.35 ENF-104 PC6 strain data before and after crack growth

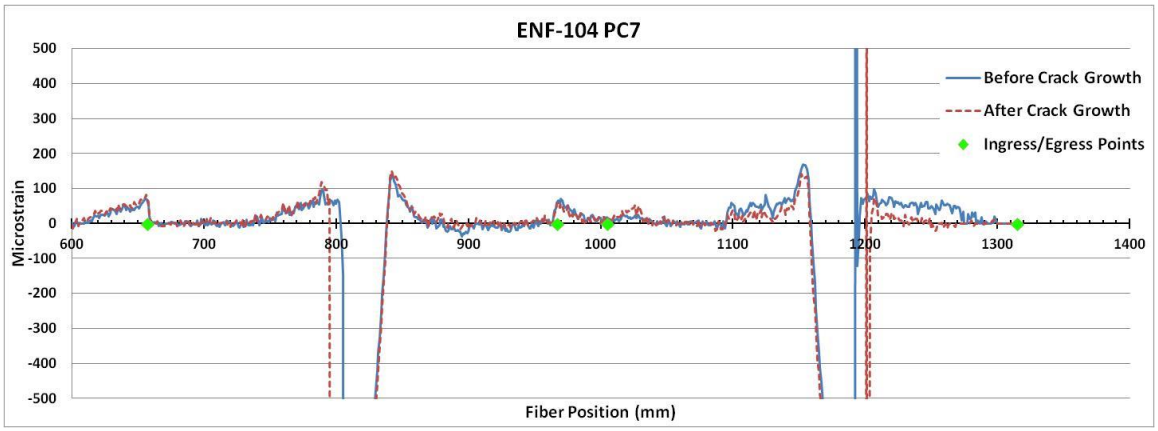

Figure B.36 ENF-104 PC7 strain data before and after crack growth

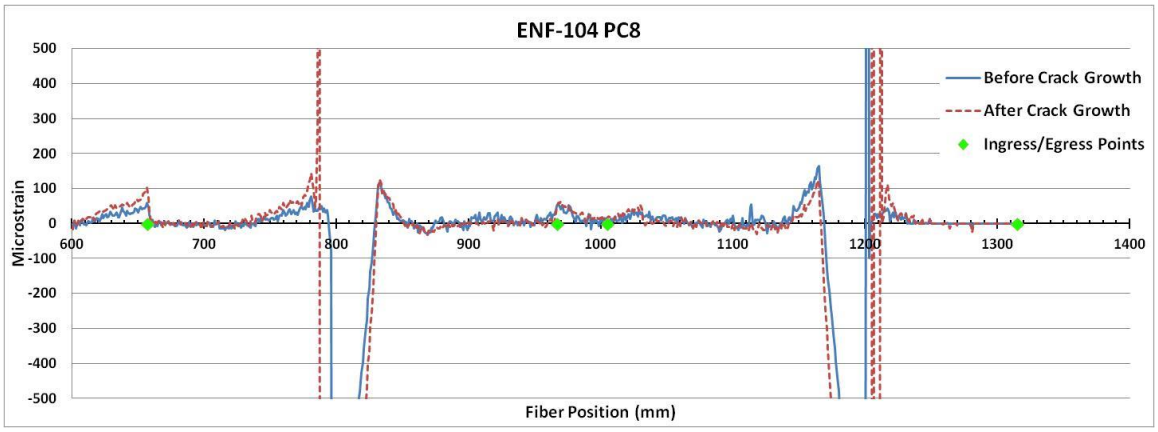

Figure B.37 ENF-104 PC8 strain data before and after crack growth

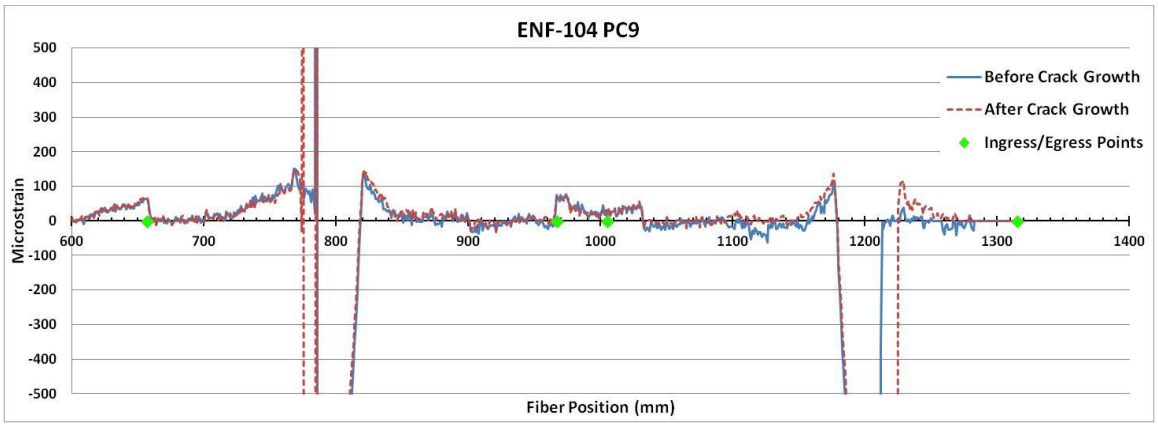

Figure B.38 ENF-104 PC9 strain data before and after crack growth

APPENDIX C

ADDITIONAL ENF CRACK FRONT MAPPING RESULTS

C.1 ENF Specimen 102

Table C.1 ENF-102 crack growth measurements (mm) for 3 mm gauge length and 3 mm spacing

	Pass 1		Pass 2		Pass 3 (middle)	
	a true	**a fiber**	**a true**	**a fiber**	**a true**	**a fiber**
NPC	23	25	23	26	24	26
PC1	18	19	18	20	18	20
PC2	16	17	16	15	16	17
PC3	16	15	16	16	16	16
PC4	15	14	15	15	15	14
PC5	13	12	12	13	13	13
PC6	15	15	15	15	16	17
PC7	13	14	14	14	14	14
PC8	14	14	14	15	14	17
PC9	12	12	13	13	12	14
				Average Difference		**0.98**
				Standard Deviation		**0.81**

Table C.2 ENF-102 crack growth measurements (mm) for 3 mm gauge length and 1 mm spacing

	Pass 1		Pass 2		Pass 3 (middle)	
	a true	**a fiber**	**a true**	**a fiber**	**a true**	**a fiber**
NPC	23	25	23	26	24	26
PC1	18	17	18	18	18	19
PC2	16	15	16	15	16	14
PC3	16	16	16	17	16	16
PC4	15	14	15	14	15	15
PC5	13	13	12	13	13	13
PC6	15		15		16	
PC7	13	12	14	13	14	13
PC8	14	12	14	13	14	13
PC9	12		13		12	
				Average Difference		**0.91**
				Standard Deviation		**0.64**

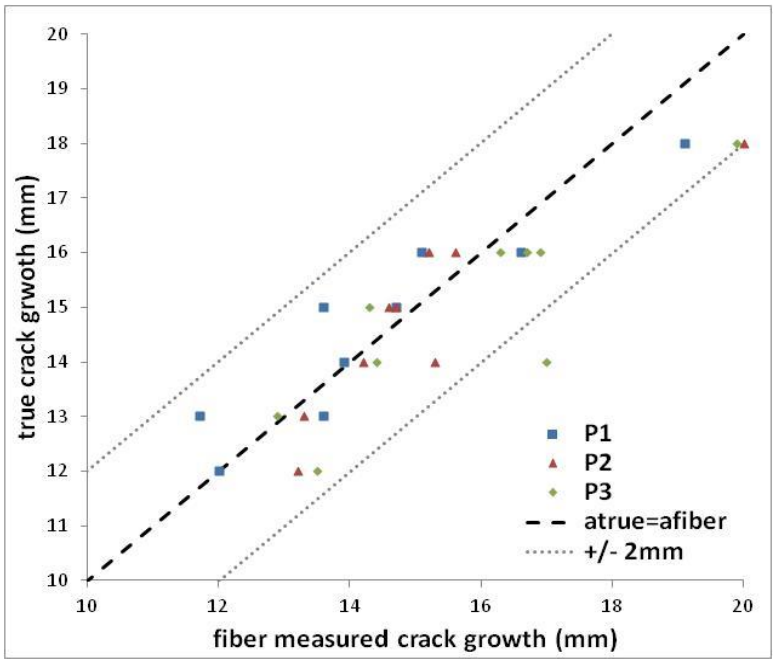

(a)

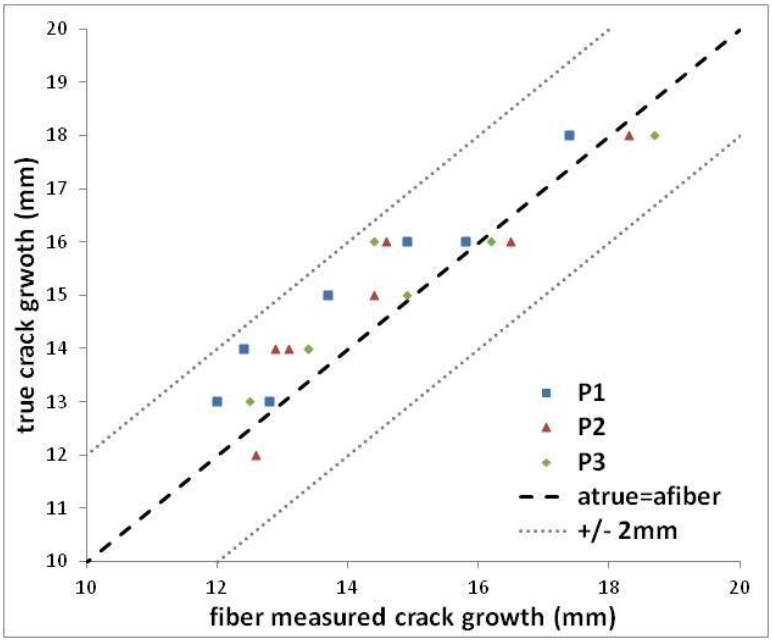

(b)

Figure C.1 Comparison of true and fiber measured crack growth for specimen ENF-102 with (a) 3 mm gauge length and 3 mm spacing and (b) 3 mm gauge length and 1 mm spacing

C.2 ENF Specimen 103

Table C.3 ENF-103 crack growth measurements (mm) for 3 mm gauge length and 3 mm spacing

	Pass 1 (middle)		Pass 2		Pass 3	
	a true	a fiber	a true	a fiber	a true	a fiber
NPC	26	28	26	28	25	25
PC1	19	18	20	19	19	16
PC2	15	14	16	15	15	12
PC3	17	16	18	15	17	14
PC4	15	14	15	15	15	13
PC5	17	15	17	15	17	14
PC6	16	17	15	15	16	16
PC7	15	16	14	15	15	14
PC8	14	14	13	15	14	14
PC9	15	14	15	14	15	14
				Average Difference		**1.4**
				Standard Deviation		**0.86**

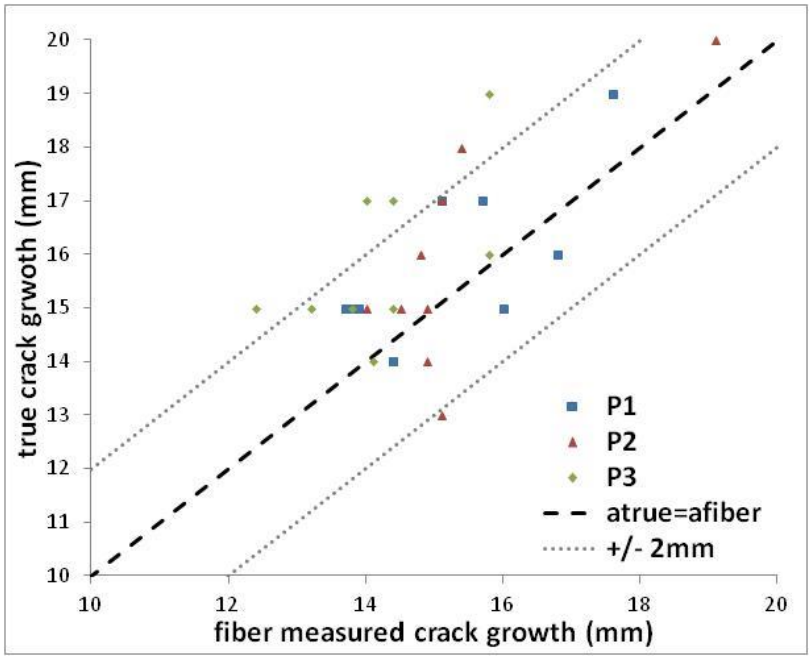

Figure C.2 Comparison of true and fiber measured crack growth for specimen ENF-103 with 3 mm gauge length and 3 mm spacing

C.3 ENF Specimen 104

Table C.4 ENF-104 crack growth measurements (mm) for 3 mm gauge length and 3 mm spacing

	Pass 1 (middle)		Pass 2	
	a true	**a fiber**	**a true**	**a fiber**
NPC	22	23	22	24
PC1	15	16	18	20
PC2	20	20	21	21
PC3	15	15	18	16
PC4	15		16	
PC5	15	15	18	19
PC6	13	12	16	16
PC7	13	12	16	16
PC8	15	16	16	16
PC9	14	13	16	16
		Average Difference		**0.7**
		Standard Deviation		**0.53**

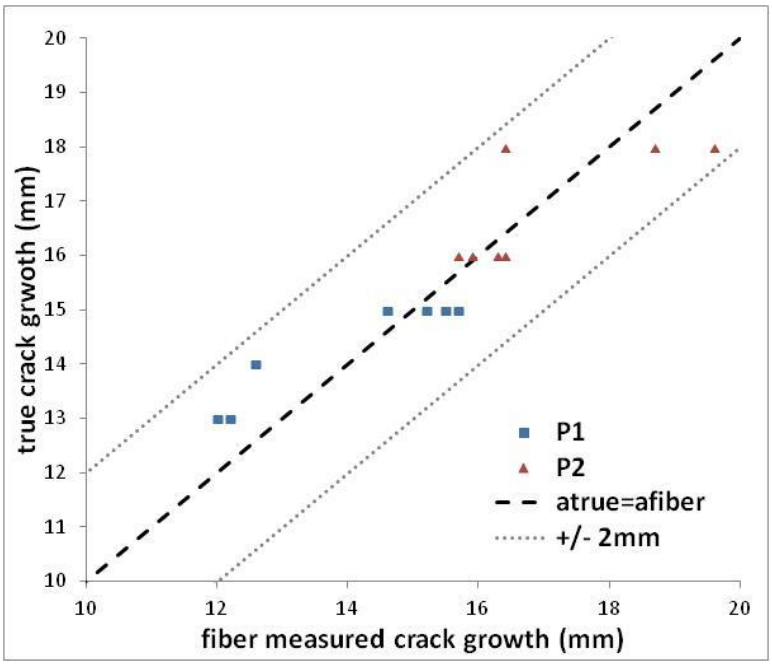

Figure C.3 Comparison of true and fiber measured crack growth for specimen ENF-103 with 3 mm gauge length and 3 mm spacing